On the use of different constitutive models in data assimilation for slope stability

Mohsan, Muhammad; Vardon, Philip J.; Vossepoel, Femke C.

DOI
10.1016/j.compgeo.2021.104332

Publication date
2021

Document Version
Final published version

Published in
Computers and Geotechnics

Citation (APA)
Mohsan, M., Vardon, P. J., & Vossepoel, F. C. (2021). On the use of different constitutive models in data assimilation for slope stability. *Computers and Geotechnics*, *138*, Article 104332. https://doi.org/10.1016/j.compgeo.2021.104332

Computers and Geotechnics 138 (2021) 104332

Contents lists available at ScienceDirect

Computers and Geotechnics

journal homepage: www.elsevier.com/locate/compgeo

On the use of different constitutive models in data assimilation for slope stability

Muhammad Mohsan, Philip J. Vardon *, Femke C. Vossepoel

Department of Geoscience and Engineering, Delft University of Technology, Stevinweg 1, 2628 CN Delft, the Netherlands

ARTICLE INFO

Keywords:
Ensemble Kalman filter
Constitutive models
Mohr-Coulomb
Hardening soil
Factor of safety
Slope stability model

ABSTRACT

A recursive ensemble Kalman filter (EnKF) is used as the data assimilation scheme to estimate strength and stiffness parameters simultaneously for a fully coupled hydro-mechanical slope stability analysis. Two different constitutive models are used in the hydro-mechanical model: the Mohr-Coulomb (MC) model and the Hardening Soil (HS) model. The data assimilation framework allows the investigation of the effect of constitutive behaviour on its ability to estimate the factor of safety using measurements of horizontal nodal displacement at the sloping face. In a synthetic study, close-to-failure and far-from-failure cases of prior property estimations illustrate the effect of initial material property distribution with different material models. The results show that both models provide a reliable factor of safety when the distribution of prior parameters is selected close-to-failure. However, the HS model results in the improved estimation of factor of safety for the far-from-failure case while this is not the case for the MC model. In addition, for the same level of accuracy the computational effort required for the HS model is comparatively less than for the MC model.

1. Introduction

The stability of slopes is important for the construction and risk assessment of infrastructure. Man-made slopes are present in many applications, such as flood protection, transport infrastructure and open-pit mining, and the potential failure of these slopes can pose a significant risk.

There are a variety of methods to assess slope stability, e.g. limit equilibrium methods, numerical methods, empirical methods and probabilistic methods. With the development of numerical methods, such as the finite element method (FEM), it has become possible to analyse and predict the behaviour of geometrically complex slopes under hydro-mechanical non-steady-state conditions. The applicability of this type of analysis significantly depends upon the constitutive (stress-strain) behaviour of the material and the mathematical representation of the behaviour used in FEM.

In the past few decades, there have been significant developments in constitutive models. For example, the evaluation of non-linearity in elasticity, elasto-plasticity and hardening/softening are now regularly seen in more advanced constitutive models. Commercial software packages (e.g. PLAXIS) offer the possibility to include different constitutive models, for example, a formulation representing linear-elastic perfectly plastic behaviour based on Mohr-Coulomb assumptions, or a hardening soil model, which is a more advanced non-linear elasto-plastic soil model that includes hardening (Plaxis, 2015).

While numerical models have been shown to capture the hydro-mechanical processes occurring in soils, the representation of slope behaviour by numerical models often differs from what is observed in reality. This can be due to a poor representation of the physical processes (either in the governing equations or in the constitutive model), poorly known model parameters, a complex geometry, complex initial and boundary conditions, or a combination of these. To investigate or overcome these limitations, one can make use of measured behaviour of the slope. Measurements can be used in two ways: one way is to compare the numerical model output with the measurements and choose the best model formulation, and an alternative way is to assimilate the measurements in a mathematically consistent way to find the most likely state and parameters given the measurements and the uncertainty in both model and measurements.

In order to evaluate the performance of constitutive models from a comparison with measurements, several studies compare the displacement produced by different constitutive models with field measurements for a range of geomechanical problems (e.g. Brinkgreve et al., 2006; Hsiung and Dao, 2014; Sekhavatian and Choobbasti, 2018).

---

* Corresponding author.
E-mail addresses: M.Mohsan@tudelft.nl (M. Mohsan), P.J.Vardon@tudelft.nl (P.J. Vardon), F.C.Vossepoel@tudelft.nl (F.C. Vossepoel).

https://doi.org/10.1016/j.compgeo.2021.104332
Received 17 March 2021; Received in revised form 25 June 2021; Accepted 27 June 2021

Brinkgreve et al. (2006) demonstrate the functioning of three constitutive models for a tunnel system. The authors compared field settlement and heave with FEM results which use the Mohr-Coulomb (MC) model, the Hardening soil (HS) model and the Hardening soil with small-strain stiffness (HSS) model. The authors conclude that the HSS model simulates the most realistic settlement and heave for this case. Hsiung and Dao (2014) studied the performance of the MC, HS and HSS models (Plaxis, 2015) for an excavation case. The authors compare the wall deflection and ground settlement with field data and conclude that the displacement produced by the HSS model is closest to the field measurements. Sekhavatian and Choobbasti (2018) compare movement prediction by FEM with field measurements in an underground excavation case. The authors compare the results produced by a number of different material models with field measurements as an indication of model performance. However, this information was not used to refine or estimate the model parameters.

As model parameters are often not well known, adjusting the parameters to values closer to the actual values can significantly improve model performance. This is often done manually as part of model calibration. An alternative way to use measurements is an inverse analysis or data assimilation approach to estimate the poorly known model parameters. Possible measurements for these approaches include surface displacements, pore water pressure and stress or strain. For example, Ledesma et al. (1996) and Gens et al. (1996) utilised a maximum-likelihood method to estimate the Young's modulus for a tunnel excavation simulation in FEM. Lee and Kim (1999) utilised an extended Bayesian method in a simulation of a tunnel system for an inverse analysis of four parameters: elastic modulus, initial horizontal stress at rest, cohesion and friction angle.

Zhou et al. (2007) proposed and implemented an extended Bayesian approach on an embankment and an excavation case. The author estimated Young's modulus for both the cases. Wang et al. (2013) conducted a probabilistic inverse analysis for a slope-failure case in Taiwan, which included soil anchors. They estimated the strength parameters and anchor force in order to better understand the slope failure mechanism. Vardon et al. (2016) and Liu et al. (2018) used an ensemble Kalman filter (EnKF) approach on a slope-stability problem. The authors combined the random finite element method (RFEM) with the EnKF to estimate the hydraulic conductivity based on pore water pressure measurements in a steady-state and transient state seepage problem in a synthetic case. The improved estimation of hydraulic conductivity led to improved pore water pressure estimation, thereby improving the prediction of slope stability. Another example of inverse analysis is provided by Kim and Finno (2020), who optimise model parameters of a hypoplastic clay model in the case of an excavation using the measurements of lateral movements at an early stage of excavation with a gradient approach based on the Gauss-Newton method.

The majority of the studies mentioned above utilised a data assimilation approach to estimate either stiffness or strength parameters. The sole estimation of stiffness parameters does not give any information about the ultimate limit state of the system (factor of safety). On the other hand, the sole estimation of the strength parameters does not give sufficient insight into the pre-failure behaviour of the material, and reduces the ability of the data to be used to estimate the strength parameters. The objective of the present study is to explore the use of data assimilation to improve estimates of slope stability by assimilating the slope deformation measurements. To this end, simultaneous estimation of the stiffness and strength parameters are conducted for two different constitutive models that incorporate material non-linearity. The evaluation of the slope-stability estimates will eventually support the development of a data assimilation framework for robust assessment of slope-failure risks.

In this study, the effect of constitutive models on the calculation of the factor of safety is addressed by assimilating the measurements into the FEM simulation of a slope stability problem, under unsteady hydraulic conditions. A comparison of close-to-failure and far-from-failure prior parameter estimation cases helps to investigate the effect of material non-linearity in two different constitutive models. A recursive EnKF is implemented for two different constitutive models (HS and MC). The performance of the resulting data assimilation systems is evaluated by their ability to estimate the horizontal displacement within the model domain and to predict the Factor of Safety (FoS) of the slope. In Section 2, details of the forward model and the data assimilation method are presented. Section 3 presents an evaluation method and a synthetic example to evaluate the system's performance, with the results presented in Section 4. Section 5 presents the discussion followed by conclusions. An investigation of the system's sensitivity to various inputs is given in Appendix A and an algorithm for the Python data assimilation interface with PLAXIS is given in Appendix B.

2. Methodology

The method is made up of a forward model which simulates the physics of the problem, and a data assimilation method that combines this forward model with measurements to estimate constitutive model parameters and the corresponding state variables. A fully coupled hydro-mechanical FEM simulation is used as the forward model. In order to investigate the effect of constitutive models on the estimated state and the estimated FoS, two types of constitutive models are used, *i.e.*, the MC and the HS models. A recursive EnKF is used as the data assimilation method to estimate the constitutive model parameters (e.g. friction angle, cohesion, stiffness) based on measurements (i.e. surface displacements). The workflow in this study is controlled via Python, making use of the PLAXIS Python interface to control the PLAXIS analyses. The FEM equations are solved by PLAXIS and the data assimilation part is implemented and solved in Python (see Appendix B for details).

2.1. Forward model

2.1.1. Fully coupled hydro-mechanical slope stability model

In soils under unsteady flow, both the mechanical and hydraulic behaviour must be considered. For the mechanical behaviour, equilibrium is considered, i.e.:

$$\nabla\cdot\boldsymbol{\sigma}' + \nabla p + \rho \boldsymbol{b} = \mathbf{0}, \tag{1}$$

where ∇ is the gradient operator, $\nabla\cdot$ is the divergence, $\boldsymbol{\sigma}'$ is the effective stress tensor, p is the pore pressure, ρ is the density and $\boldsymbol{b}$ are the body accelerations (e.g. from gravity).

The constitutive behaviour can be expressed as:

$$\boldsymbol{\sigma}' = \mathbf{D}'\epsilon \tag{2}$$

where $\mathbf{D}'$ is the effective constitutive matrix and ϵ is the strain tensor.

By substituting Eq. 2 into Eq. 1 and recognising that $\epsilon = 0.5((\nabla \boldsymbol{u}) + (\nabla \boldsymbol{u})^T)$ (where $\boldsymbol{u}$ is the displacement) yields the mechanical governing equation. The displacement is resolved into its x- and y-components and termed as horizontal displacements ($\boldsymbol{u}_x$) and vertical displacements ($\boldsymbol{u}_y$), respectively.

For the hydraulic behaviour, the governing equation is the conservation of mass which can be expressed as:

$$\frac{\partial(\rho_l n)}{\partial t} = -\nabla\cdot\boldsymbol{v} - Q \tag{3}$$

where ρ_l is the fluid density, n is the porosity, $\boldsymbol{v}$ is the velocity vector and Q is a source term. The derivative of the fluid density with time is calculated using the compressibility of the fluid ($\partial\rho_l/\partial t = \rho_l/K_w\cdot\partial p/\partial t$, where K_w is 2183 MPa) and the change of porosity is evaluated from the change of the volumetric strain ϵ_{vol}.

The velocity of water is incorporated via Darcy's Law:

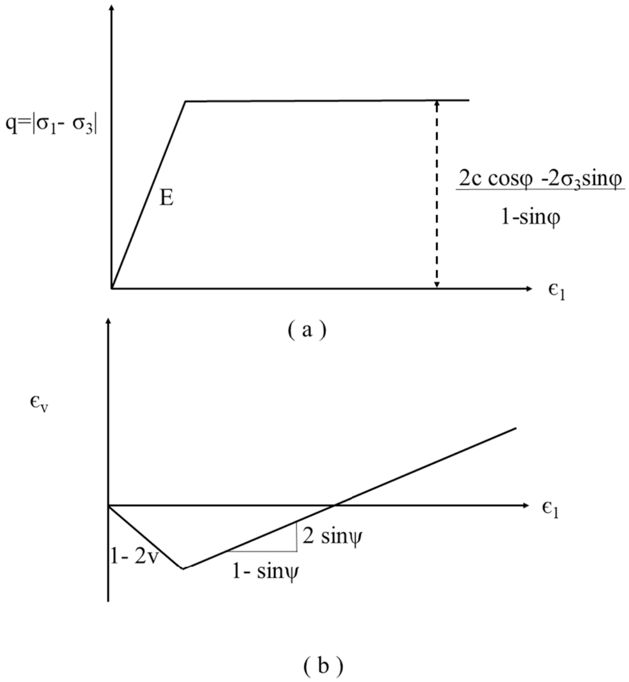

Fig. 1. Representation of Mohr-Coulomb model.

$$\boldsymbol{v} = -\mathbf{k}\nabla\left(\frac{p}{\rho_l g} + z\right) \tag{4}$$

where $\mathbf{k}$ is the hydraulic conductivity matrix, g is the gravitational constant, and z is the elevation.

Both the governing equations have primary variables of displacement and fluid pressure, and are therefore a coupled system of equations. In this work, the governing equations are solved using FEM by using the software PLAXIS (Plaxis, 2015).

2.1.2. *Constitutive models*

Stress-strain (constitutive) relationships of real soils are usually non-linear. The stiffness and shear strength of soil typically depends upon the stress level, the strain level and the stress history. A variety of constitutive models exists to simulate soil behaviour. In this study, two types of constitutive models are used *i.e.* the Mohr-Coulomb (MC) model and the Hardening Soil model (HS). The MC model is commonly used in geotechnical analyses as it is simple and represents stress-dependent failure conditions reasonably well, but misses some realistic soil features, *i.e.* non-linear elasticity, stress-dependent stiffness, hardening/softening and plasticity before failure. On the other hand, the HS model takes into account these realistic features but is not as frequently used in geotechnical practice, partly due to the requirement of additional parameters.

Mohr-Coulomb model: The MC model is a simple and well known linear-elastic perfectly-plastic model, which is used widely to represent soils. The linear elastic part of the Mohr-coulomb model is based on Hooke's law, and is therefore not stress or strain dependent, and the

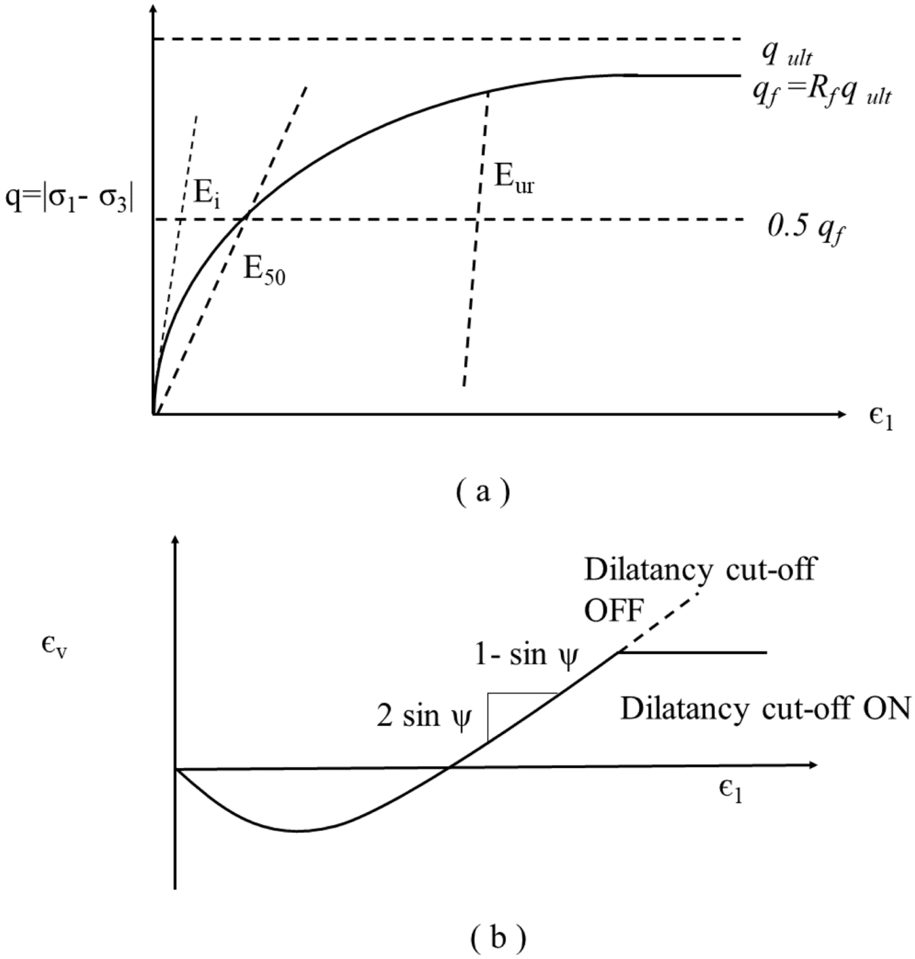

Fig. 2. Representation of Hardening soil model.

onset of plasticity is based on the Mohr-Coulomb failure criterion, *i.e.* a stress-dependent shear strength. Plastic deformations occur without any change in stress level, *i.e.* they are perfectly plastic. This also implies that the model is non-associated. A representation of the model is shown in Fig. 1.

A total of five model parameters are required to implement the Mohr-Coulomb model. This includes the two elastic parameters, the Young's modulus (E), Poisson's ratio (ν), and three strength parameters, cohesion (c), friction angle (ϕ) and dilatancy angle (ψ).

Hardening Soil model: The HS model is a nonlinear elasto-plastic soil model. The stress-strain relationship in a drained triaxial compression test is represented by the hyperbolic function (Fig. 2). The model shows a decreasing stiffness (stress-dependent stiffness) and irreversible plastic strains simultaneously when subjected to deviatoric loading. Three different stress-dependent stiffness parameters are considered to model soil behaviour. The stress-strain path due to primary loading is curved, which is modelled using E_{50}, the stress-dependent stiffness due to the primary loading.

$$E_{50} = E_{50}^{ref}\left(\frac{c\cos(\phi) - \sigma_3\sin(\phi)}{c\cos(\phi) - p_{ref}\sin(\phi)}\right)^m, \tag{5}$$

where E_{50}^{ref} is the reference stiffness modulus corresponding to the reference stress p_{ref}. The actual stiffness depends upon the minor principal stress (σ_3). The amount of stress dependency is given by the power m.

The non-linear elastic part is modelled based upon the stress-dependent unloading reloading stiffness modulus:

$$E_{ur} = E_{ur}^{ref}\left(\frac{c\cos(\phi) - \sigma_3\sin(\phi)}{c\cos(\phi) - p_{ref}\sin(\phi)}\right)^m, \tag{6}$$

where E_{ur}^{ref} is the reference re/-unloading stiffness at reference pressure p_{ref}. The E_{ur} parameter is used to simulate the non-linear unloading reloading stress-strain path. The elastic components are calculated according to the Hookean elastic relationship for drained triaxial stress path:

$$\epsilon_1^e = \frac{q}{E_{ur}}. \tag{7}$$

The HS model is a double-hardening plasticity model as it allows two types of hardening: shear hardening and cap hardening. The shear-hardening part controls the hyperbolic behaviour in deviatoric stress paths, and the cap-hardening part deals with irreversible compaction in primary compression. Due to the onset of loading, the material starts yielding as soon as the shear strength is mobilised. As a result, increased deviatoric plastic strain is generated as the loading increases, which apparently leads to a reduction of the stiffness. This is represented by the shear hardening yield function. At the end of shear strength mobilisation, when the Mohr-Coulomb failure criterion is reached, failure occurs. The flow rule for shear hardening is non-associated.

A cap yield surface is defined to compute the plastic volumetric strain that is measured in isotropic compression. This yield surface represents an ellipse in stress space and it is centred around the origin of the stress space. The preconsolidation pressure defines the current position of the cap. The evolution of preconsolidation pressure with volumetric strain is formulated by a hardening rule which reads:

$$E_{oed} = E_{oed}^{ref}\left(\frac{c\cos(\phi) - \sigma_3'\sin(\phi)}{c\cos(\phi) - p_{ref}\sin(\phi)}\right)^m, \tag{8}$$

where E_{oed}^{ref} is the reference odometer stiffness at reference pressure p_{ref}.

The input parameters of the HS model are the strength parameters: cohesion (c), friction angle (ϕ) and dilatancy angle (ψ). The stiffness parameters are the secant stiffness at reference pressure in standard drained triaxial test (E_{50}^{ref}), the tangent stiffness at reference pressure for primary odometer loading (E_{oed}^{ref}), the loading unloading stiffness at reference pressure (E_{ur}^{ref}), the Poisson's ratio for unloading reloading (ν_{ur}) and a parameter m which controls the stress-level dependency for all three stiffness parameters.

2.1.3. Forward modelling and stability analysis

FEM simulations are used as a forward model, taking into account changes in external water loads. A hydro-mechanical FEM model computes the behaviour and state of the slope. After a defined period of time, the hydro-mechanical analysis is followed by the stability analysis, which results in an estimate of the FoS (the ratio of the original strength to the reduced strength of the material at failure). Slope stability is computed using FEM with a strength reduction method. The forward model calculates the results until the time when a stability analysis is required. After the stability analysis, the forward analysis resumes using the conditions immediately prior to the stability analysis. The calculated stability, therefore, can change over time reflecting the changes in hydro-mechanical conditions. In the stability analyses, the strength properties of the soil ($\tan(\phi)$ and c in both the constitutive models used here) are successively reduced until failure.

2.2. Data assimilation with the recursive ensemble Kalman filter

Data assimilation has the objective to find the posterior distribution of a state and/or parameter given the measurements of the state. A commonly used method for data assimilation is the EnKF (Evensen, 1994) which is an ensemble-based formulation of the Kalman filter (Kalman, 1960), originally developed for state estimation in oceanography. The method uses an ensemble of model realisations to represent the error covariances. Since then, EnKF has been implemented in diverse fields including numerical weather prediction (e.g. Houtekamer and Mitchell, 2005; Szunyogh et al., 2005), oceanography (e.g. Bertino et al., 2003; Keppenne and Rienecker, 2003), hydrology (e.g. Reichle et al., 2002; Chen and Zhang, 2006), geotechnical engineering (e.g. Vardon et al., 2016; Mavritsakis, 2017; Liu et al., 2018), and petroleum reservoir history matching (e.g. Evensen, 2009; Aanonsen et al., 2009; Oliver and Chen, 2011; Glegola et al., 2012; Nævdal et al., 2002).

EnKF is very effective in state estimation (e.g. Evensen, 1994; Houtekamer and Mitchell, 1998; Miller et al., 1999; Hamill et al., 2000; Tamura et al., 2014) and joint parameter-state estimation (e.g. Lorentzen et al., 2001; Nævdal et al., 2005; Nævdal et al., 2002; Skjervheim and Evensen, 2011). In the case of parameter estimation, it is common to estimate the parameters first and then rerun the model with these updated estimates of the parameters to find the solution of the model state. The EnKF has been successfully applied for parameter estimation in applications in a range of fields. In the field of petroleum engineering, Nævdal et al. (2002) implemented the EnKF for history matching with a two dimensional near-well reservoir model to estimate the permeability of the reservoir. The EnKF provided a better parameter estimation and consequently better production forecasts. In the field of atmospheric modelling, Annan et al. (2005) implemented the EnKF for estimation of parameters from radiation, convection and surface parametrisation. The authors concluded that the EnKF can handle multivariate parameter estimation comfortably and demonstrated the method to be useful in determining structural deficiencies in the model which can not be improved by tuning and can be a useful tool to guide model development. Skjervheim and Evensen (2011) applied EnKF on a history matching problem to estimate the permeability parameter in a reservoir simulation model. It was concluded that the EnKF can be successfully used for history matching but is computationally more expensive than the Ensemble Smoother. A possible disadvantage of the EnKF is the Gaussian approximation applied in the update scheme. Furthermore, the repeated restarting of the forward model after each EnKF update needs a significant amount of computational effort, this recursive implementation of the EnKF ensures that the state is updated along with the parameters. Due to the good state, parameter and combined state-parameter estimation, relative computational efficiency and the continuous and close to Gaussian distribution (or distributions which could be transformed to Gaussian), the EnKF approach has been selected. Moreover, the approach is consistent with earlier work by Vardon et al. (2016) and the present study can be seen as an extension of that work. In the present study, the recursive EnKF is implemented to estimate poorly known parameters in a hydro-mechanical slope-stability forward model.

To formulate the principles of data assimilation, it is assumed that the model output at the measurement location $\boldsymbol{y}$ is obtained by running the forward model with input model parameters $\boldsymbol{\theta}$ and mapping the outcome to measurement space. This can be represented by the operator g in the following equation:

$$\boldsymbol{y} = g(z), \tag{9}$$

in which

$$z = (\boldsymbol{x} \quad \boldsymbol{\theta})^{\mathrm{T}} \tag{10}$$

where $\boldsymbol{y} \in \mathbb{R}^{N_m}$ is a vector of model output at measurement locations, $z \in \mathbb{R}^{N_x+N_\theta}$ is a combined state-parameter vector, *i.e.*, a vector of model state $\boldsymbol{x} \in \mathbb{R}^{N_x}$ and model parameters $\boldsymbol{\theta} \in \mathbb{R}^{N_\theta}$ and g is the model operator which maps the prior state-parameter vector into measurement space. In this study, the model is considered to be perfect and model uncertainty is implicitly taken into account within the parameter uncertainty. Here, N_m is the number of measurements, N_x is the number of state points and N_θ is the number of parameters.

A forward model run provides a prediction of the model state evolution for a unique set of values of the uncertain parameters. If the model has no errors, the model output can be seen as a prediction (y) of the 'truth'. The measurements are the window to this actual state, and contain errors:

$$\boldsymbol{d} = \boldsymbol{y} + \boldsymbol{e}, \tag{11}$$

where $\boldsymbol{d} \in \mathbb{R}^{N_m}$ is a vector of the measurements with N_m being the number of measurements. The errors $\boldsymbol{e} \in \mathbb{R}^{N_m}$ include measurement errors and representation errors. In this study, measurement errors are assumed to be normally distributed with zero mean. The distribution of the state-parameter vector z is assumed to also be normally distributed around a known mean.

Bayes' theorem gives the joint probability (f) for z and $\boldsymbol{y}$ given the measurements $\boldsymbol{d}$ as:

$$f(z, \boldsymbol{y}|\boldsymbol{d}) \propto f(\boldsymbol{d}|\boldsymbol{y}) f(\boldsymbol{y}|z) f(z). \tag{12}$$

From Eq. 12, the posterior probability for z given $\boldsymbol{d}$ can be written as:

$$f\left(z|\boldsymbol{d}\right) \propto \int f\left(\boldsymbol{d}|\boldsymbol{y}\right) f\left(\boldsymbol{y}|z\right) f\left(z\right) dy = f\left(\boldsymbol{d}|g\left(z\right)\right) f\left(z\right). \tag{13}$$

Making use of the assumption that the priors have a Gaussian distribution, Eq. 13 can be written as:

$$f\left(z|\boldsymbol{d}\right) \propto \exp\left\{-\frac{1}{2}J\right\}. \tag{14}$$

The cost function J is defined as follows:

$$J\left(z\right) = \left(z - z^{\mathrm{f}}\right)^{\mathrm{T}} \mathbf{C}_{zz}^{-1} \left(z - z^{\mathrm{f}}\right) + \left(g(z) - \boldsymbol{d}\right)^{\mathrm{T}} \mathbf{C}_{dd}^{-1} \left(g\left(z\right) - \boldsymbol{d}\right), \tag{15}$$

where z^{f} is the prior estimate of z, $\mathbf{C}_{zz} \in \mathbb{R}^{(N_x+N_\theta)\times(N_x+N_\theta)}$ is the error covariance of z^{f}, and $\mathbf{C}_{dd} \in \mathbb{R}^{N_m \times N_m}$ is the error covariance of measurements. It can be shown that for normally distributed variables, the maximum likelihood estimate of $f(z|\boldsymbol{d})$ is equivalent to minimising the cost function J in Eq. 15. In case of an operator $g(z)$ that can be approximated with a linear operator $\mathbf{G}$ that relates the output to the parameters and state via $\boldsymbol{y} = \mathbf{G}z$, minimising the cost function gives the following solution, known as the Kalman filter (Kalman, 1960):

$$z^{\mathrm{a}} = z^{\mathrm{f}} + \mathbf{K}\left(\boldsymbol{d} - g\left(z\right)\right), \tag{16}$$

$$\mathbf{C}_{zz}^{\mathrm{a}} = \left(\mathbf{I} - \mathbf{K}\mathbf{G}\right)\mathbf{C}_{zz}, \tag{17}$$

and

$$\mathbf{K} = \mathbf{C}_{zz}\mathbf{G}\left(\mathbf{G}\mathbf{C}_{zz}\mathbf{G}^{\mathrm{T}} - \mathbf{C}_{zz}\right)^{-1}, \tag{18}$$

where $\mathbf{K}$ is the Kalman gain, superscript "a" shows the analysis and superscript "f" represents the prior estimate.

In EnKF, an ensemble of forward model simulations is used to approximate the error covariance $\mathbf{C}_{zz}$. The Kalman equation for each ensemble member $i \in N_{\mathrm{e}}$ can be written as:

$$z_i^{\mathrm{a}} = z_i^{\mathrm{f}} + \mathbf{K}^e\left(\boldsymbol{d}_i - g\left(z_i^{\mathrm{f}}\right)\right), \tag{19}$$

and

$$\mathbf{K}^e = \mathbf{C}_{zz}^e\mathbf{G}\left(\mathbf{G}\mathbf{C}_{zz}^e\mathbf{G}^{\mathrm{T}} - \mathbf{C}_{dd}\right)^{-1}, \tag{20}$$

where $\mathbf{C}_{zz}^e$ is the combined state-parameter error covariance matrix. Here

$$\boldsymbol{d}_i = \boldsymbol{d} + \epsilon_i \tag{21}$$

represents the perturbed measurements for each ith member, with ϵ_i having the same distribution as the measurement errors $\boldsymbol{e}$ in Eq. 11, following the approach of (Burgers et al., 1998).

Consider the matrix $\mathbf{Z}_t^{\mathrm{f}} \in \mathbb{R}^{(N_x+N_\theta)\times N_{\mathrm{e}}}$ containing N_{e} realisations of z at time t:

$$\mathbf{Z}_t^{\mathrm{f}} = \left(z_1^{\mathrm{f}}, z_2^{\mathrm{f}}, \ldots.., z_{N_{\mathrm{e}}}^{\mathrm{f}}\right) \tag{22}$$

The ensemble mean is then stored in each column of $\overline{\mathbf{Z}}_t^{\mathrm{f}} \in \mathbb{R}^{(N_x+N_\theta)\times N_{\mathrm{e}}}$:

$$\overline{\mathbf{Z}}_t^{\mathrm{f}} = \mathbf{Z}_t^{\mathrm{f}}\mathbf{I}_{N_{\mathrm{e}}}, \tag{23}$$

where $\mathbf{I}_{N_{\mathrm{e}}} \in \mathbb{R}^{N_{\mathrm{e}}\times N_{\mathrm{e}}}$ is a matrix with each element equal to $\frac{1}{N_{\mathrm{e}}}$. The ensemble perturbation matrix $\mathbf{Z}_t^{'} \in \mathbb{R}^{(N_x+N_\theta)\times N_{\mathrm{e}}}$ is now defined as follows:

$$\mathbf{Z}_t^{'} = \mathbf{Z}_t^{\mathrm{f}} - \overline{\mathbf{Z}}_t^{\mathrm{f}}. \tag{24}$$

The combined state-parameter error covariance matrix $\mathbf{C}_{zz}^e \in \mathbb{R}^{(N_x+N_\theta)\times(N_x+N_\theta)}$ can be written as follows:

$$\mathbf{C}_{zz}^e = \frac{\mathbf{Z}_t^{'}\left(\mathbf{Z}_t^{'}\right)^{\mathrm{T}}}{N_{\mathrm{e}} - 1}, \tag{25}$$

where $\mathbf{C}_{zz}^e$ consists of the state and parameter error covariances as well as the cross-covariances between state and parameters.

At assimilation time step t, the available measurements are stored in vector $\boldsymbol{d}_t$. For each ensemble member i, this measurement vector is perturbed with ϵ_i as in Eq. 21. The vectors $\boldsymbol{d}_{i,t}$ are then stored in matrix $\mathbf{D}_t \in \mathbb{R}^{N_m\times N_e}$:

$$\mathbf{D}_t = \left(\boldsymbol{d}_{1,t}, \boldsymbol{d}_{2,t}, \ldots, \boldsymbol{d}_{N_{\mathrm{e}},t}\right). \tag{26}$$

With these matrices, the analysis equation at time t becomes:

$$\mathbf{Z}_t^{\mathrm{a}} = \mathbf{Z}_t^{\mathrm{f}} + \mathbf{C}_{zz}^e\mathbf{G}^{\mathrm{T}}\left(\mathbf{G}\mathbf{C}_{zz}^e\mathbf{G}^{\mathrm{T}} + \mathbf{C}_{dd}\right)^{-1}\left(\mathbf{D}_t - \mathbf{G}\mathbf{Z}_t^{\mathrm{f}}\right), \tag{27}$$

where $\mathbf{G} \in \mathbb{R}^{N_{\mathrm{e}}\times(N_x+N_\theta)}$ is the linear measurement operator which relates the state-parameter matrix to measurement space.

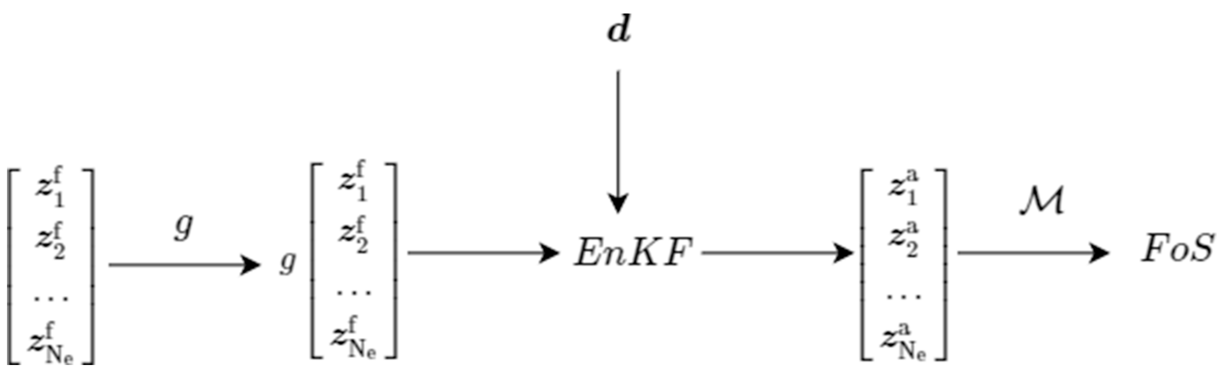

Fig. 3. Setup of the data assimilation and forward model, where $\begin{bmatrix} z_1^f & z_2^f & \dots & z_{N_e}^f \end{bmatrix}^T$ is the ensemble of prior state-parameter estimates; *g* is the model operator; *EnKF* represents the data assimilation (recursive EnKF); ***d*** is the measurement vector; $\begin{bmatrix} z_1^a & z_2^a & \dots & z_{N_e}^a \end{bmatrix}^T$ is the ensemble of posterior state-parameter estimates; and $\mathcal{M}$ is the FoS calculation.

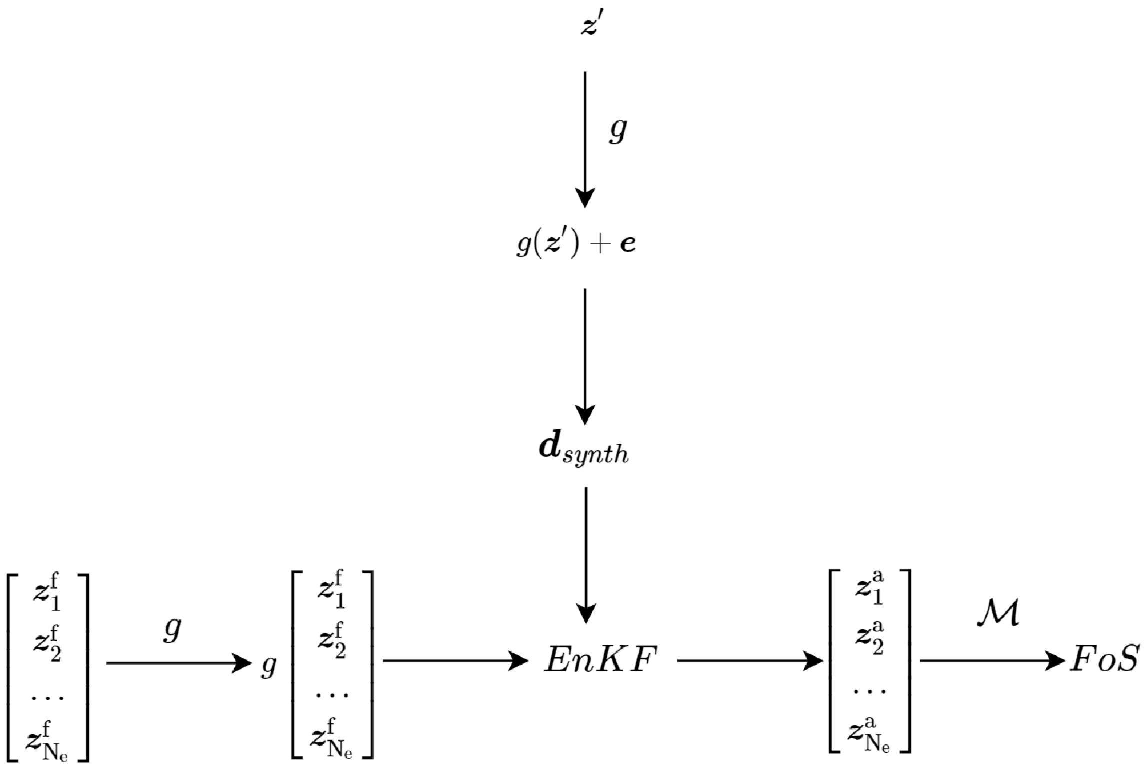

Fig. 4. Setup of the data assimilation and forward model in a synthetic twin experiment, where z' is the state-parameter vector used to create synthetic observations; ***e*** is normally distributed measurement noise; $\boldsymbol{d}_{synth}$ is the vector containing synthetic measurements; For all other symbols, please see Fig. 3.

2.3. Implementation of the data assimilation for the slope-stability problem

In this study, the EnKF described in Section 2.2 is implemented with the forward model of Section 2.1. The resulting model for the hydro-mechanical behaviour of given slope geometry is then used to estimate the state ($\boldsymbol{x}$), parameters ($\boldsymbol{\theta}$) and eventually the FoS. The state in the case of this setup, could be displacements of the sloping surface, or observed strain. Parameters would represent the material properties in the hydro-mechanical model simulation and could be for example the parameters of stiffness and strength, $E/E_{50}^{ref}, c'$ and ϕ'. The selection of state and parameters to estimate this particular study will be discussed in Section 3. The setup of the numerical approach is illustrated in Fig. 3.

At $t = 0$, the numerical approach starts with a set of prior ensemble members which represent our prior assumption of the state ($\boldsymbol{x}$) and parameters ($\boldsymbol{\theta}$). In our case, these model parameters ($\boldsymbol{\theta}$) are sampled from a normal distribution with a prior mean and standard deviation for each of the parameters in $\boldsymbol{\theta}$:

$$f(\boldsymbol{\theta}) = \mathcal{N}(\boldsymbol{\theta}^f, \mathbf{C}_{\theta\theta}) \tag{28}$$

Based on the prior assumptions on parameters, the forward model is run from $t = 0$ to $t = t_{assim}$. The synthetic measurements at $t = t_{assim}$ are assimilated to estimate model parameters ($\widehat{\boldsymbol{\theta}}$) and state variable ($\widehat{\boldsymbol{x}}$), defined as the expected value of the posterior distribution. In the synthetic experiment, the modelled field measurements are sampled from the vector z by means of the operator **G** which maps the state-parameter space to the measurement space. As **G** in this case combines the forward model operator with an interpolation of the model variables to the location of the measurements at the slope, the interpolation in **G** has the form of $[\mathbf{I}|\mathbf{0}]$ which has "1" only at specified locations. $\mathbf{C}_{dd} \in \mathbb{R}^{N_m \times N_m}$ in Eq. 27 is in this case a matrix with all the diagonal elements equal to the

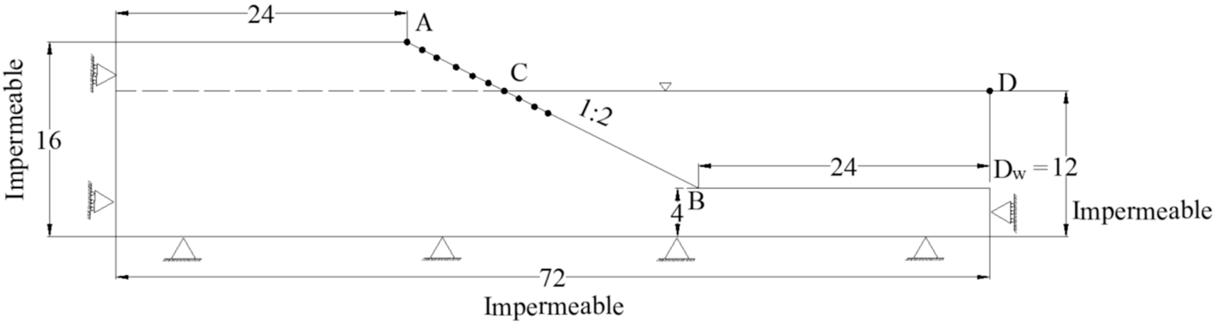

Fig. 5. Geometry of the slope (dimensions in m) and black circles represents the measurement points.

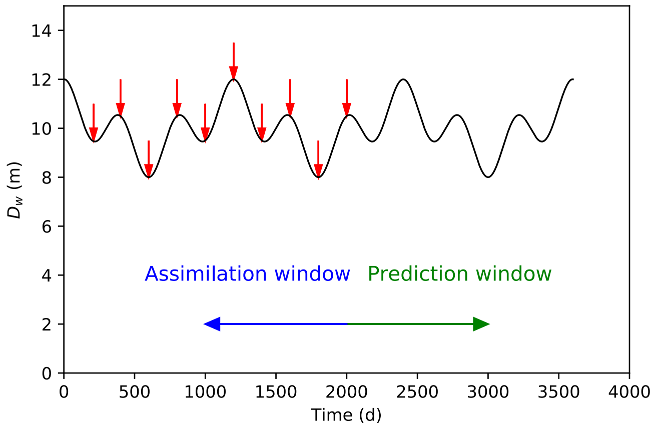

Fig. 6. Fluctuation of the water (D_W) level in CD. The red arrows represent the assimilation points.

Table 1
Parameter variation and average sensitivity score (AvSS) for MC and HS.

Parameter variations			AvSS (%)	
E/E_{50}^{ref} (kPa)	ϕ’ (°)	$c^{'}$ (kPa)	MC	HS
$\theta_{E/E_{50}^{ref},min} = 10000$, $\theta_{E/E_{50}^{ref},max} = 40000$	27	10	45.44	37.62
30000	$\theta_{\phi,min} = 20$, $\theta_{\phi,max} = 35$	10	42.77	48.53
30000	27	$\theta_{c,min} = 5$, $\theta_{c,max} = 15$	11.78	13.84

variance of the measurement device. After each EnKF update, the forward model is rerun from $t = 0$ to next assimilation step to keep the model state consistent with the parameter estimates of the previous step. The measurements at the next assimilation step are assimilated to update the model state and parameter estimates. In this way, the data is assimilated for all the time steps. The resulting posterior ensemble of state- and parameter estimates is then used for the calculation of the FoS.

3. Synthetic twin experiment

A synthetic twin experiment is a common approach to evaluate the performance of data assimilation methods. In this experiment, synthetic measurements are generated from a synthetic “truth” data-set, which mimics the observed reality. The data assimilation should reconstruct this “truth” within the assumed accuracy of the measurements. The “truth” is the output from a specific simulation of the forward model with a certain initial state and specified model parameters, typically different from the mean of the prior distribution of the state and parameter estimates of the ensemble used in the data assimilation. By sampling measurements of the “true” state from the output of the simulation and after adding realistic noise, synthetic measurements are obtained. The concept of a synthetic twin experiment is illustrated in Fig. 4.

An idealised slope has been considered to illustrate and test the approach. The geometry of the slope is shown in Fig. 5. The initial stress state of the slope system is calculated by using gravity loading and the initial pore-water pressure distribution is calculated assuming steady-state groundwater flow considering the water level *CD*. Above the line *CD*, the degree of saturation is determined by the soil water retention curve. This hydraulic behaviour of the unsaturated soil is modelled by the model of Van Genuchten (1980). Following the initial stress state, the slope experiences a water level fluctuation of the line *CD*, which is included via a variable hydraulic boundary condition. The water level fluctuation has been simulated by applying $D_w = 12 - (\sin t + \sin 3t)$, where t is the time in days and D_w is the water level in meters from the bottom of the slope (see Fig. 6). The change of hydraulic loading are the only cause of deformations and are obtained from the fully coupled hydro-mechanical analysis. Synthetic measurements are obtained by sampling the model output of horizontal displacements ($\boldsymbol{u_x}$) at the sloping face (along the line *ACB*) and adding realistic noise to mimic geodetic measurements. For this study, synthetic measurements are sampled at the peaks and troughs of D_w and at regular intervals of 200 days (see red arrows in Fig. 6). These synthetic measurements are assimilated after 200, 400, 600, 800, 1000, 1200, 1400, 1600, 1800 and 2000 days.

Both the MC and HS models are used in separate analyses to test their influence on the results. The stiffness and (effective) strength parameters are decided to be estimated simultaneously, as plasticity (although no full plastic mechanism) can occur prior to failure. This allows both the serviceability limit state and ultimate limit state (slope reliability) to be investigated. To decide which parameters to estimate in the data assimilation, an average sensitivity score (*AvSS*) is calculated to study the effect of model parameters ($E/E_{50}^{ref}, c^{'}$ and ϕ’) on the horizontal nodal displacements at the slope. First, the sensitivity score (*SS*) for each parameter i is calculated by:

$$SS_i = \frac{100\left|F(\theta_{i,max}) - F(\theta_{i,min})\right|}{\sum_{j=1}^{n}\left|F\left(\theta_{j,max} - F\left(\theta_{j,min}\right)\right)\right|} \tag{29}$$

where θ_i is a certain parameter ($E/E_{50}^{ref}, c^{'}$ or ϕ’). The *SS* gives the parameter’s sensitivity, $F(\theta_{i,max})$ is the model output (in our case horizontal nodal displacement at sloping face) when $\theta_i = \theta_{i,max}, F(\theta_{i,min})$ is the model output when $\theta_i = \theta_{i,min}$ and n is the total number of parameters varied to study the sensitivity. While studying the sensitivity of a specific parameters the other parameters are kept constant. The *AvSS* is calculated by averaging the *SS* for all time steps. The parameter variation and *AvSS* can be seen in Table 1. It can be concluded from Table 1 that in the case of the MC model E and ϕ’ and, in the case of HS model E_{50}^{ref} and ϕ’

Table 2
"Truth" model parameters for MC and HS.

Parameters	Truth model parameters		Unit
	MC	HS	
Effective friction angle (ϕ')	25	25	°
Effective cohesion (c')	10	10	kPa
Dilatancy angle (ψ)	0	0	°
Young's modulus (E)	20000	–	kPa
E_{50}^{ref}	–	20000	kPa
E_{oed}^{ref}	–	E_{50}^{ref}	kPa
E_{ur}^{ref}	–	$3E_{50}^{ref}$	kPa
Poisson's ratio (ν)	0.3	–	–
Poisson's ratio for unloading/reloading (ν_{ur})	–	0.2	–
Power (m)	–	0.5	–
Unsaturated unit weight (γ_d)	19	19	kN/m^3
Saturated unit weight (γ_s)	20	20	kN/m^3
Hydraulic conductivity ($k_x = k_y$)	1.0	1.0	m/day
VGM parameter (g_a)	3.83	3.83	m^{-1}
VGM parameter (g_n)	1.3774	1.3774	–
VGM parameter (g_l)	1.25	1.25	–
Saturated volumetric water content (θ_s)	0.403	0.403	–
Residual volumetric water content (θ_r)	0.025	0.025	–

*Note: VGM stands for Van Genuchten model and the properties are taken from Wösten et al. (1999).

are the parameters which have the highest sensitivity. Hence, these parameters are selected to be estimated in this study. This means that $\boldsymbol{\theta} = (E \quad \phi')^{\mathrm{T}}$ in the MC case and $\boldsymbol{\theta} = \left(E_{50}^{ref} \quad \phi'\right)^{\mathrm{T}}$ in the HS case. The state variable ($\boldsymbol{x}$) for both cases is horizontal nodal displacements ($\boldsymbol{u_x}$).

The input model parameters for the synthetic measurements are shown in Table 2, which result in an initial factor of safety of 1.50 for both models representing the synthetic "truth". To evaluate the two constitutive models, two separate numerical experiments are selected for each model: a close-to-failure and a far-from-failure prior parameter estimation. The synthetic measurements in both experiments are identical, but the prior ensemble of the synthetic close-to-failure case has a mean factor of safety of close to 1.0 while the prior ensemble of the synthetic far-from-failure case has a mean factor of safety of close to 2.0. The input model parameters for prior parameter estimation are shown in Table 3. The model parameters to be estimated, *i.e.*, the stiffness (E or E_{50}^{ref}) and the strength (ϕ') parameters, are sampled from their prior distributions to form the prior model ensemble.

A fully coupled hydro-mechanical analysis is conducted from $t = 0-200$ days for each ensemble member. The horizontal nodal displacement vector ($\boldsymbol{u_x}$) is stored in a forecast matrix (see Eq. 22) for each ensemble member. Then, available synthetic measurements of horizontal nodal displacement at $t = 200$ days are assimilated by using the recursive EnKF. The output of the EnKF provides a new estimation of the E/E_{50}^{ref} and ϕ' for each ensemble member as well as the model state. The model parameters (E/E_{50}^{ref} and ϕ') are then used in the fully coupled hydro-mechanical analysis from the initial stage ($t = 0$) until the time of the next available measurements ($t = 400$ days). These measurements are then assimilated to update the estimates of model parameters. This process is repeated until all data has been assimilated.

The data is assimilated for the first 2000 days after which the forward model provides an estimate of horizontal displacement and FoS for the period from 2000 days to 3600 days. The setup uses fifty ensemble members for the comparison of the two constitutive models. The ensemble size, the number of measurements and simulated measurement error are based on sensitivity analyses (Appendices A.1–A.3).

4. Results of the data assimilation

4.1. Displacement estimates

In this section, the posterior horizontal nodal displacement ($\boldsymbol{u_x}$) estimates based on the prior and estimated parameters are presented. Fig. 7 shows the prior and posterior ensemble of horizontal nodal displacement at point A (see Fig. 5) for the four different cases. This data is one of the measurements used for the data assimilation. The blue lines represent the ensemble prediction of horizontal nodal displacement at point A based on the prior ensemble of parameters (see Table 3), with the heavy blue line representing the mean. The red lines show the ensemble prediction based on the estimated parameters at 2000 days. The green stars are the synthetic measurements at point A for different time steps. The time period is divided into an assimilation and a prediction window. The black dashed line represents the true displacement at point A.

The results of horizontal nodal displacement show a sinusoidal behavior, due the variable hydraulic boundary conditions. Overall, the spread of the horizontal nodal displacement of the prior ensemble (shown in blue lines) is larger than that of the estimated ensemble parameters at 2000 days (shown in red lines) in all cases. By comparing the results of close-to-failure case for the MC and the HS models, it can be seen that displacement of the HS model analysis (Fig. 7c) is larger than the displacement from the MC model analysis (Fig. 7a). This is due to the stress-dependent stiffness in the prior HS ensemble. Due to an increase in loading, the stiffness reduces and shear strength starts mobilizing results in the larger displacements. On the other hand, this is not the case in the MC ensemble which has single stress-independent stiffness parameter and perfect plasticity develops at failure. The spread in the prior distribution of the ensemble displacement is also larger for the HS model than for the MC model.

In the far-from-failure case, the analysis shows that the model produces a smaller displacement than in the close-to-failure case (see Figs. 7a and 7b or Figs. 7c and 7d). This is because the strength properties are higher in far-from-failure, and therefore plastic deformation is very limited.

4.2. Material parameter estimates

In this section, the estimation of poorly known parameters are presented at different time steps. Fig. 8 shows the true stiffness (E/E_{50}^{ref}) parameters, the initial distribution of stiffness (E/E_{50}^{ref}) parameters and the estimated stiffness (E/E_{50}^{ref}) parameters after 1000 days and 2000 days for the close-to-failure case. The mean posterior estimate of the stiffness (E/E_{50}^{ref}) approaches the true stiffness and its posterior variance reduces with each assimilation step. At 1000 days, the estimated stiffness (E) mean and standard deviation for MC case is $\mu_E = 20663$ and $\sigma_E = 1642$. In case of the HS model, the mean and standard

Table 3
Initial estimation of model parameters for MC and HS.

Parameters	Close-to-failure case	Far-from- failure case	Distribution	Unit
Effective friction angle (ϕ')	$\mu = 20, \sigma = 3$ (both)	$\mu = 35, \sigma = 2$ (both)	Normal	°
Young's modulus (E)	$\mu = 25000, \sigma = 5000$ (MC)	$\mu = 25000, \sigma = 5000$ (MC)	Normal	kPa
E_{50}^{ref}	$\mu = 25000, \sigma = 5000$ (HS)	$\mu = 25000, \sigma = 5000$ (HS)	Normal	kPa

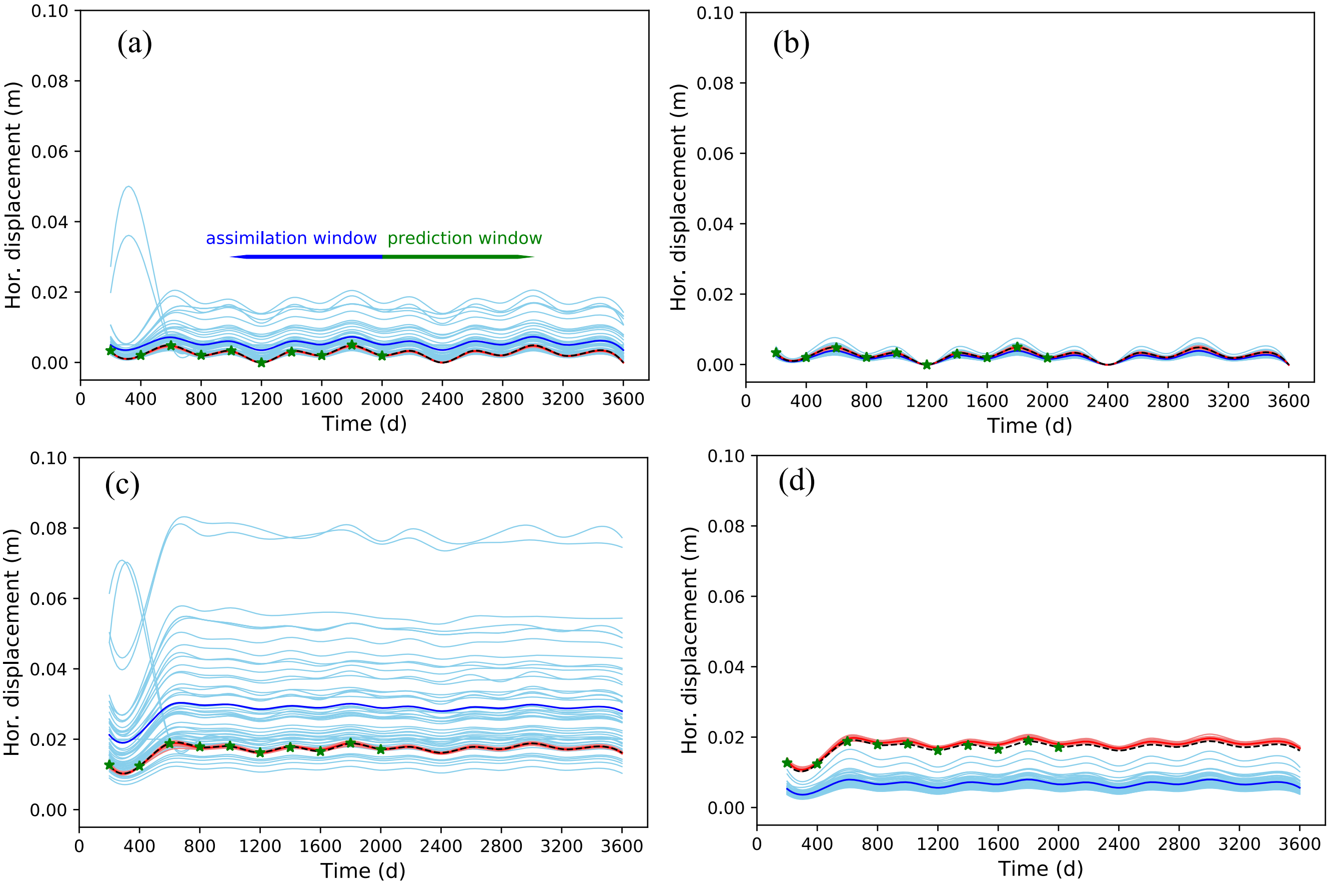

Fig. 7. Ensemble prediction of the horizontal displacement based on (i) the prior ensemble of parameters (blue lines) and (ii) estimated parameters at 2000 days, after all data have been assimilated (red lines). Green stars represent the measurements in assimilation window and the black dashed line represents the true displacement at point A of the slope.

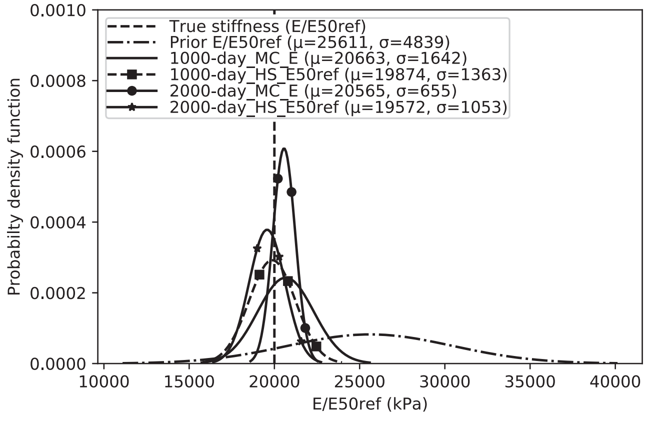

Fig. 8. Estimation of stiffness parameter for the MC and HS soil models at t = 1000 and t = 2000 days (close-to-failure).

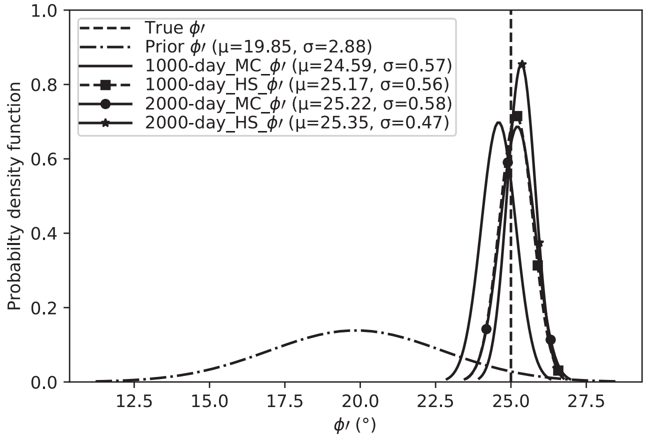

Fig. 9. Estimation of friction angle for the MC and HS soils model at t = 1000 and t = 2000 days. Two curves (1000-day_HS_ϕ' and 2000-day_MC_ϕ') are overlapping in this figure (close-to-failure).

deviation of stiffness (E_{50}^{ref}) at 1000 days is $\mu_{E_{50}^{ref}} = 19874$ and $\sigma_{E_{50}^{ref}} = 1363$. At 2000 days, the estimated mean stiffness and standard deviations for the MC and the HS model simulations are $\mu_E = 20565$ and $\sigma_E = 655$ and $\mu_{E_{50}^{ref}} = 19572$ and $\sigma_{E_{50}^{ref}} = 1053$, respectively. Fig. 9 shows that effective strength parameter (ϕ') for both models improves substantially during the first 1000 days, and changes less after that. The response of both models is similar for close-to-failure case.

Figs. 10 and 11 show the parameter estimation for far-from-failure case. Fig. 10 shows that the mean of the stiffness parameters (E/E_{50}^{ref}) also approaches towards the true stiffness and shows the similar trend as of close-to-failure case for both the MC and the HS model. Fig. 11 shows the initial and estimated effective strength parameter (ϕ') at 1000 days and 2000 days. The effective strength parameter (ϕ') does not improve in the case of MC model. However, the effective strength parameter (ϕ') significantly improves in estimates of the HS model and the posterior ensemble mean approaches the true solution. The effectiveness of the data assimilation is likely related to the dependence of the stiffness E_{50}^{ref} to the effective strength parameter (ϕ') (see Eq. 5) as well as the dependence of horizontal nodal displacement to stiffness and strength

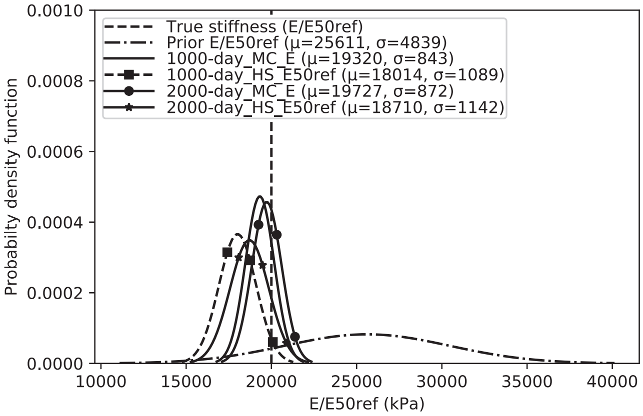

Fig. 10. Estimation of stiffness for the MC and HS soil models at t = 1000 and t = 2000 days (far-from-failure).

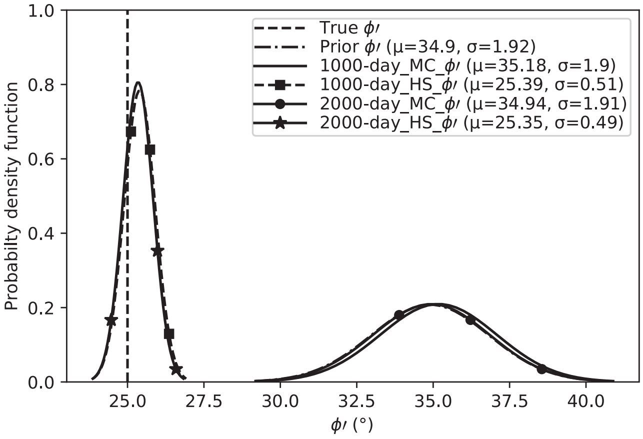

Fig. 11. Estimation of friction angle for the MC and HS soil models at t = 1000 and t = 2000 days. Two curves (1000-day_HS_ϕ' and 2000-day_HS_ϕ') are overlapping on the left side and three curves (Prior ϕ', 1000-day_MC_ϕ' and 2000-day_MC_ϕ') are overlapping on the right side of figure (far-from-failure).

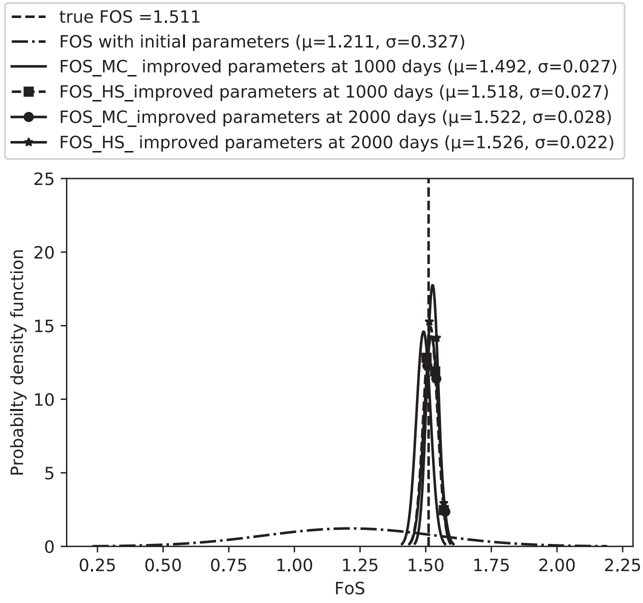

Fig. 12. Probability distribution of factor of safety at 2000 days based on the prior and estimated parameters at 1000 and 2000 days (close-to-failure).

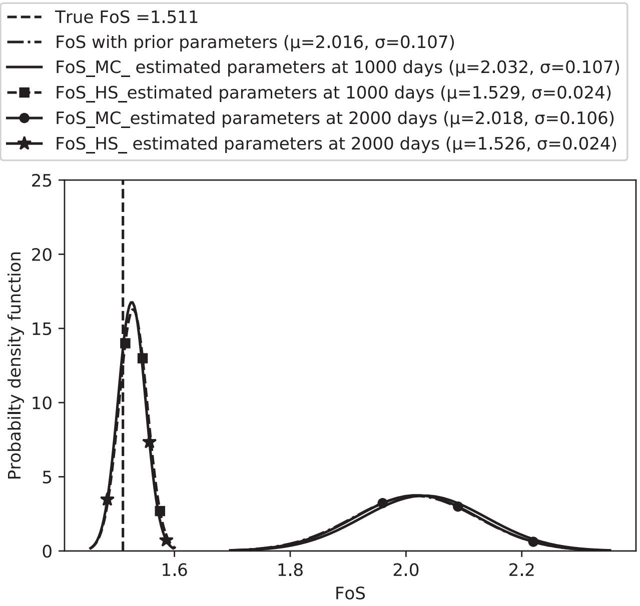

Fig. 13. Probability distribution of factor of safety at 2000 days based on the prior and estimated parameters at 1000 and 2000 days. Two curves (FoS_HS_estimated parameters at 1000 days and FoS_HS_estimated parameters at 2000 days) are overlapping on the left side and three curves (FoS with prior parameters, FoS_MC_estimated parameters at 1000 days and FoS_MC_estimated parameters at 2000 days) are overlapping on the right side of the figure (far-from-failure).

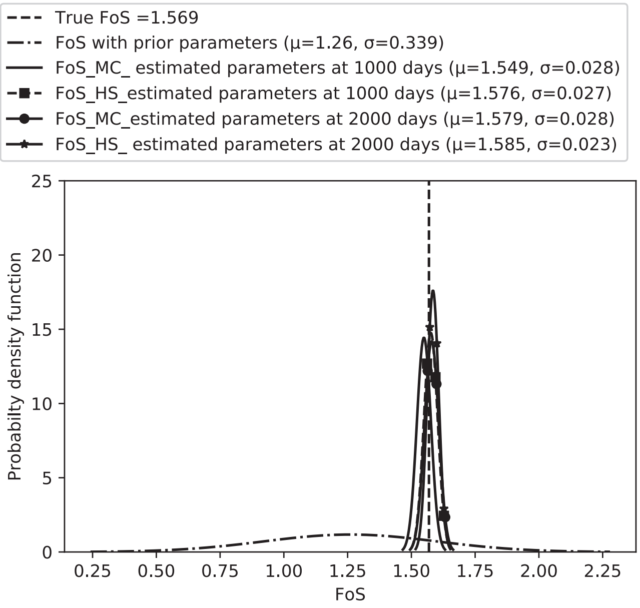

Fig. 14. Probability distribution of factor of safety at 3000 days based on the prior and estimated parameters at 1000 and 2000 days (close-to-failure).

parameters at all stages in the HS model, whereas there is no dependence between these parameters in the MC model. In the MC model far-from-failure case, only very limited plasticity occurs in the ensemble members, leading to a negligible (or zero) cross-correlation between the effective strength parameter (ϕ') and horizontal nodal displacement (u_x) in the covariance matrix (see Eq. 25).

4.3. Factor of safety

The ultimate objective of this study is to improve the estimate of the FoS making use of available measurements of slope deformation.

Figs. 12 and 13 show the FoS distributions for the two models at 2000 days with the prior parameters and the parameters estimated using data until 1000 and 2000 days. In the close-to-failure case (see Fig. 12), the FoS estimated from the model simulation with the prior parameters has a distribution with mean (μ_{FoS})= 1.26 and standard deviation (σ_{FoS})= 0.327. With parameters estimated at 1000 days and 2000 days, only very limited differences are observed between the factors of safety as calculated using the two constitutive models. Both models show a substantial effect of the data assimilation on the FoS estimate, giving a better approximation of the true FoS, and resulting in a posterior FoS estimate with a small variance. Often slopes are required to be assessed against a target reliability, and a narrower disitribution of FoS suggests a higher reliability. This will likely have a positive effect on the assessment of this FoS against a target reliability. In the far-from-failure case, similar behaviour of the FoS estimation is observed as in the case of the estimation of the strength parameter (ϕ') in Section 4.2, *i.e.*, the MC model results are substantially unaffected by the data assimilation, remain far from the truth and have a broader distribution of the posterior estimate of the FoS. As a consequence, in the far-from-failure case, the slope reliability of the MC model does not appear to be realistic, despite of the assimilation of measurements of displacement.

To demonstrate the behaviour of the models during the prediction window, the factor of safety is plotted at 3000 days in Fig. 14 for the close-to-failure case for both material models. It can be seen that the posterior estimate of the factor of safety remains stable throughout the prediction window. This is not surprising, considering the stable behaviour of the simulations during this time (Fig. 7) and the fact that there are no temporal material behaviour or geometry changes in the model.

5. Discussion

The above analyses reveal a number of key points regarding the use of data assimilation in geotechnical analyses. For most realistic slopes (FoS$<\approx 3$), the results suggest that there is scope with relatively limited stress perturbations to improve reliability estimations using displacement measurements.

With the MC model, the most commonly used geotechnical material model, horizontal displacement has no dependence on the strength parameters in the elastic region, this means that these parameters have dependence only if sufficient plasticity is occurring, *i.e.*, in the close-to-failure case. A good estimate of the prior ensemble is needed for this material model, given that there needs to be a dependence on the displacement and the strength properties, in the representation of the model error covariance of the assimilation scheme (Eq. 25). In contrast, the HS model has a dependence of the elastic behaviour on the strength parameters (Eqs. 5, 6, 8), which means that even with a prior estimation that is less accurate, the data assimilation will be effective. This result stresses the importance of choosing a constitutive model for data assimilation which is able to characterise the typical interplay between strength (as represented by the friction angle parameter) and stiffness.

It can also seen that the number of measurements and number of ensemble members is able to be lower for the HS model (Appendices A.1 and A.3). This may be counter-intuitive, given that it is more complex and resembles more realistic geotechnical behaviour, however this is likely due to the stronger correlation between the strength and stiffness parameters in the HS model. Both of these effects will have the impact of reducing computational effort of the analyses, which will be significant in more complex analyses.

The notion that, especially in the case of the HS model, the assimilation of measurements of displacement leads to more realistic estimates of the strength and stiffness parameters and the associated nodal displacement in the slope, already after a small number of assimilation steps, suggests that the use of data assimilation techniques for slope-reliability estimates are promising. It should be noted though, that this study describes a synthetic case only, and assumed values of measurement errors have optimistic values. A more realistic configuration with more realistic model properties will require further study. Specifically, the spatial variability of materials within the slope has not been taken into account, and it is thought that this will have an impact, in particular on the required number of measurement points. Moreover, the temporal sampling of the measurements in this study has been regular and beneficial for the reconstruction of the temporal variations of the deformation. Additional research would be required to investigate the performance of the data assimilation setup under different measurement conditions.

Key limitations of this approach (EnKF) include (i) the Gaussian approximation in the update scheme, which means that the EnKF is difficult to implement on non-Gaussian problems; (ii) the recursive nature of the recursive EnKF, which results in restarting realizations after each parameter update step, which can be computationally expensive. In this study, computational expenses are furthermore increased by the need to run ensemble realizations sequentially due to the way licenses of PLAXIS software are linked to specific computational nodes.

6. Conclusion

The influence of two different constitutive models on factor of safety is studied by using data assimilation with the recursive ensemble Kalman filter in a slope stability model. In a synthetic twin experiment that mimics a slope geometry and assimilates synthetic measurements of slope deformation into a hydro-mechanical model, the use of the Mohr-Coulomb and the Hardening Soil models is tested. The HS model is seen to estimate the factor of safety with a narrow posterior distribution, starting from a wide prior distribution of material parameters, including those not encompassing the actual parameters. For this calculation, the HS model requires less computational effort than the MC model for similar or even more accurate estimates of horizontal displacement. The results suggest that constitutive models which have an influence of the strength behaviour in the elastic zone, e.g. those which include a smooth transition between elastic and plastic zones, are more effective in data assimilation schemes than those in which the relation between stiffness and strength parameters is less well represented. When choosing a constitutive model that captures these relations, the results of this study suggest that the use of data assimilation techniques for slope-reliability estimates offers the opportunity to improve slope-reliability estimates with relatively limited stress perturbations.

CRediT authorship contribution statement

Muhammad Mohsan: Conceptualisation, Methodology, Data curation, Formal analysis, Visualisation, Investigation, Writing - original draft. **Philip J. Vardon:** Conceptualisation, Funding acquisition, Methodology, Investigation, Writing - review & editing, Supervision. **Femke C. Vossepoel:** Conceptualisation, Funding acquisition, Methodology, Investigation, Writing - review & editing, Supervision.

Declaration of Competing Interest

The authors declare that they have no known competing financial interests or personal relationships that could have appeared to influence the work reported in this paper.

Acknowledgements

The authors would like to thank Dr. M. Buxton for the supervision, and Dr. R. Brinkgreve and Dr. A. P. van den Eijnden for their fruitful discussions/suggestions. The first author also would like to thank Elahe Jamalinia and Kancharla Varun Choudary for their help related to PLAXIS. This work is part of the research programme i2Mon project number 800689, funded via the EU HORIZON 2020 Research Fund for Coal and Steel (RFCS) programme.

Appendix A. Sensitivity of the displacement estimates to the data assimilation setup

A sensitivity analysis is conducted to study the influence of number of measurements, measurement error and ensemble size on the numerical data assimilation setup to the displacement estimates. In order to evaluate the final results, the normalised root mean square error (NRMSE) is calculated for the horizontal nodal displacement in the entire model domain. Considering that the root mean square error *RMSE* of horizontal nodal displacement (in meters) is given by:

$$RMSE = \sqrt{\frac{1}{N_{u_x}} \sum_{i=1}^{N_{u_x}} \left(u_{x_i^t} - u_{x_i^e} \right)^2}. \tag{30}$$

The NRMSE is given by:

$$NRMSE = \frac{RMSE}{RMSE_i} \tag{31}$$

where N_{u_x} is the total number of unknown horizontal displacements in the slope, *i.e.*, the number of nodes in the model, $u_{x_i^t}$ is the true horizontal nodal displacement at node *i* and $u_{x_i^e}$ is the estimated horizontal nodal displacement at this node. The normalised root mean square error (NRMSE) is the ratio between the RMSE and its value for the prior RMSE estimate. The normalisation facilitates the comparison of the resulting deformations of different magnitudes. The lower the NRMSE, the closer the result is to the true displacement. It should be kept in mind that the expected value of the difference between $ux_i^t - ux_i^e$ should in the ideal case be equal to the measurement error. In this section, the sensitivity analysis for the close-to-failure case is presented, *i.e.*, the case where the prior ensemble of parameters have been selected such, that the slope is in a condition close to failure. Note that while studying the sensitivity of one factor of the data assimilation setup, the other factors are kept constant.

A.1. Sensitivity to the number of measurements

In order to choose the required number of measurements in data assimilation scheme for the model comparison, several cases with different number of measurements are selected. Fig. 15 shows the NRMSE for different number of measurements (*m*) for the MC and the HS model. All

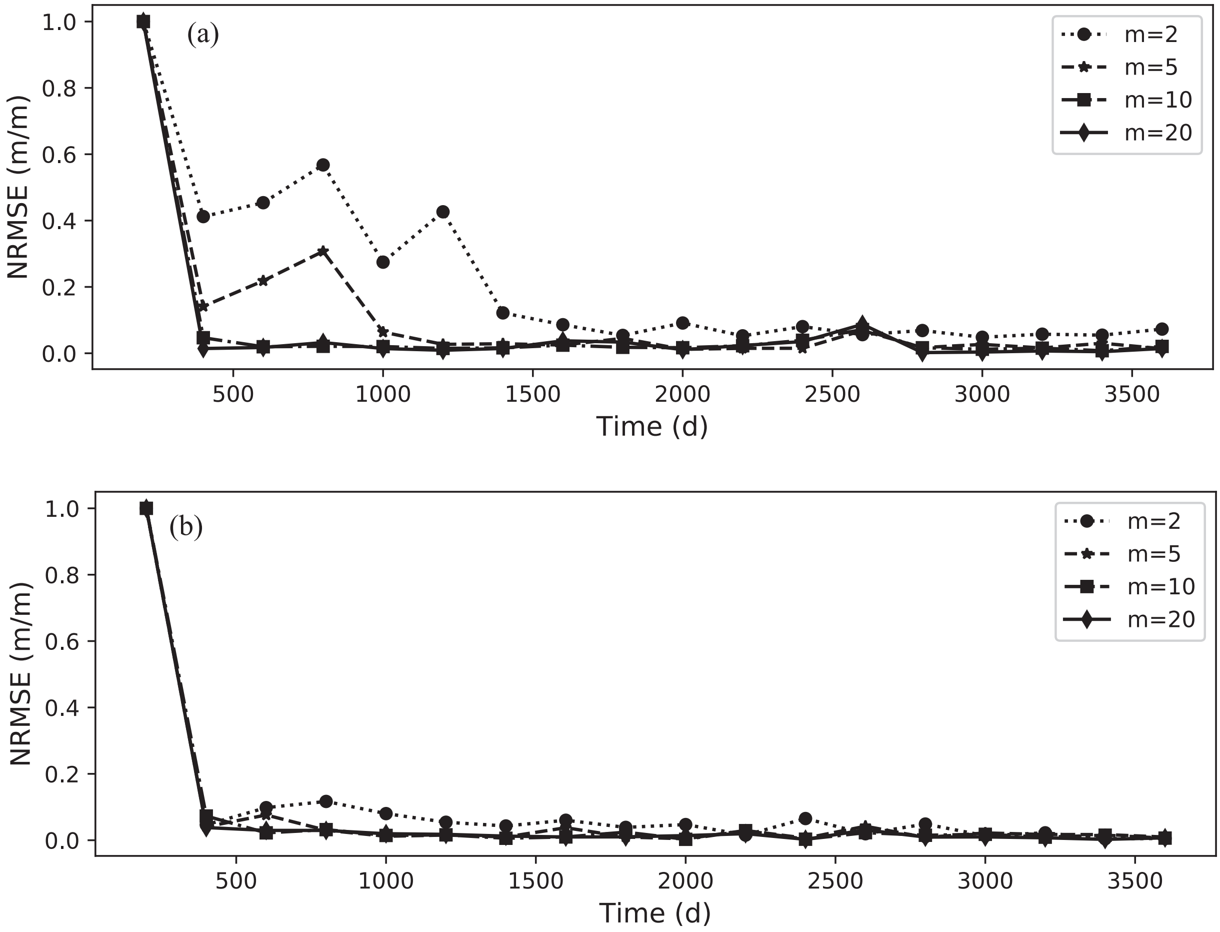

Fig. 15. RMSE estimation of the horizontal nodal displacement for different number of measurements for the (a) MC and (b) HS material models.

measurement points are located on the sloping face starting from point A towards C (see Fig. 5). A set of $m = 2$, 5, 10 and 20 measurements is selected to study the sensitivity of the horizontal displacement estimate to the number of measurements. Fig. 5 illustrates the location of the measurements for the number of measurements $m = 10$. The NRMSE for all nodal points in the mesh geometry is plotted against the time, and is seen to generally decrease with time, meaning that after each assimilation step, the resulting deformation estimate is closer to the truth.

It can be seen from Fig. 15a that the NRMSE for the MC case converges more slowly towards the expected value for the NRMSE when $m = 2$ and $m = 5$. Some fluctuations in the NRMSE values are observed with this number of measurements. However, in the case of $m = 10$ and $m = 20$, the solution quickly approaches the expected value of the NRMSE, with the majority of the improvement occurring within the first data assimilation steps. In case of the HS model, the NRMSE of the estimated horizontal displacement does not fluctuate (see Fig. 15b). The NRMSE reaches its expected value even with a relatively low number of measurements ($m = 2$ or 5). It can be seen from Fig. 15 that m>=10 appears to be an effective choice for the number of measurements for both models. Because of this, a value of $m = 10$ was used in Section 4 of this study.

A.2. Sensitivity to the measurement error

In order to study the effect of the measurement error, several experiments are performed with different measurement error variance. Fig. 16 shows the NRMSE of horizontal nodal displacement resulting from different choices of the measurement error variance ϵ. In case of the MC model (see Fig. 16a), it can be seen that the when the error variance is 10^{-5} m^2, the NRMSE fluctuates, but does not converges towards the expected value of the NRMSE, which should be for each case equal to the value of ϵ chosen for that case. For error variance of 10^{-6} m^2, the NRMSE still fluctuates. For error variances less than 10^{-6} m^2, the solution is seen to quickly approach its expected value.

In case of the HS model (see Fig. 16b), the NRMSE fluctuates when the error variance is 10^{-5} m^2, but with a significantly lower level than for the MC model. When the error variance is less than 10^{-6} m^2, a satisfactory solution is obtained. For both models, the horizontal displacement approximates the true horizontal displacement within the assumed error margin when the error is less than 10^{-7} m^2. In a realistic case, measurements of deformations at the slope would be available from geotechnical devices (inclinometer, laser sensor, extensometer) or geodetic measurements (levelling, InSAR or laser). With current geodetic/geotechnical measurement techniques (e.g. Hou et al., 2005; Lovas et al., 2008; Abellán et al., 2009) it is realistic to measure at an accuracy of $\approx$1 mm (equivalent to an error variance of 10^{-7} m^2), therefore a value of 10^{-7} m^2 measurement error is assumed in Section 4 of this study.

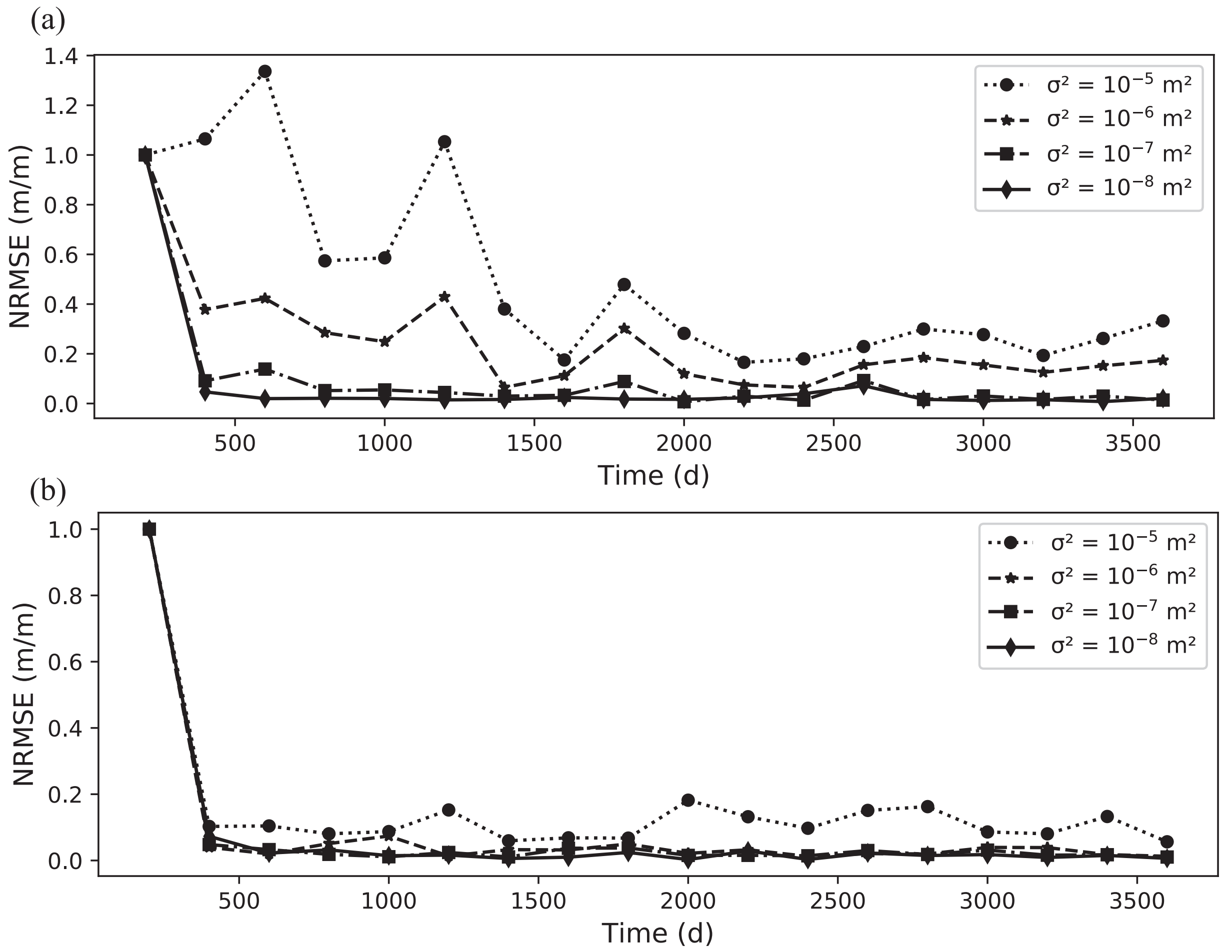

Fig. 16. RMSE estimation of the horizontal nodal displacement for different choices of the measurement error variance for the (a) MC and (b) HS material models.

A.3. Ensemble size

Several cases with different ensemble members (N_e) are used to study the influence of different ensemble sizes on the estimate of the horizontal nodal displacement in the mesh of the synthetic slope. Fig. 17 shows the NRMSE resulting from different ensemble sizes. In case of the MC model (Fig. 17a), the NRMSE reduces to around 10% of the prior RMSE and then oscillates when the number of ensemble members is less than 50. In case of the HS model (Fig. 17b), the NRMSE converges towards the expected value of the NRMSE with ensemble members, $N_e \geqslant 30$. For this reason, an ensemble size of $N_e = 50$ is selected in Section 4 of this study.

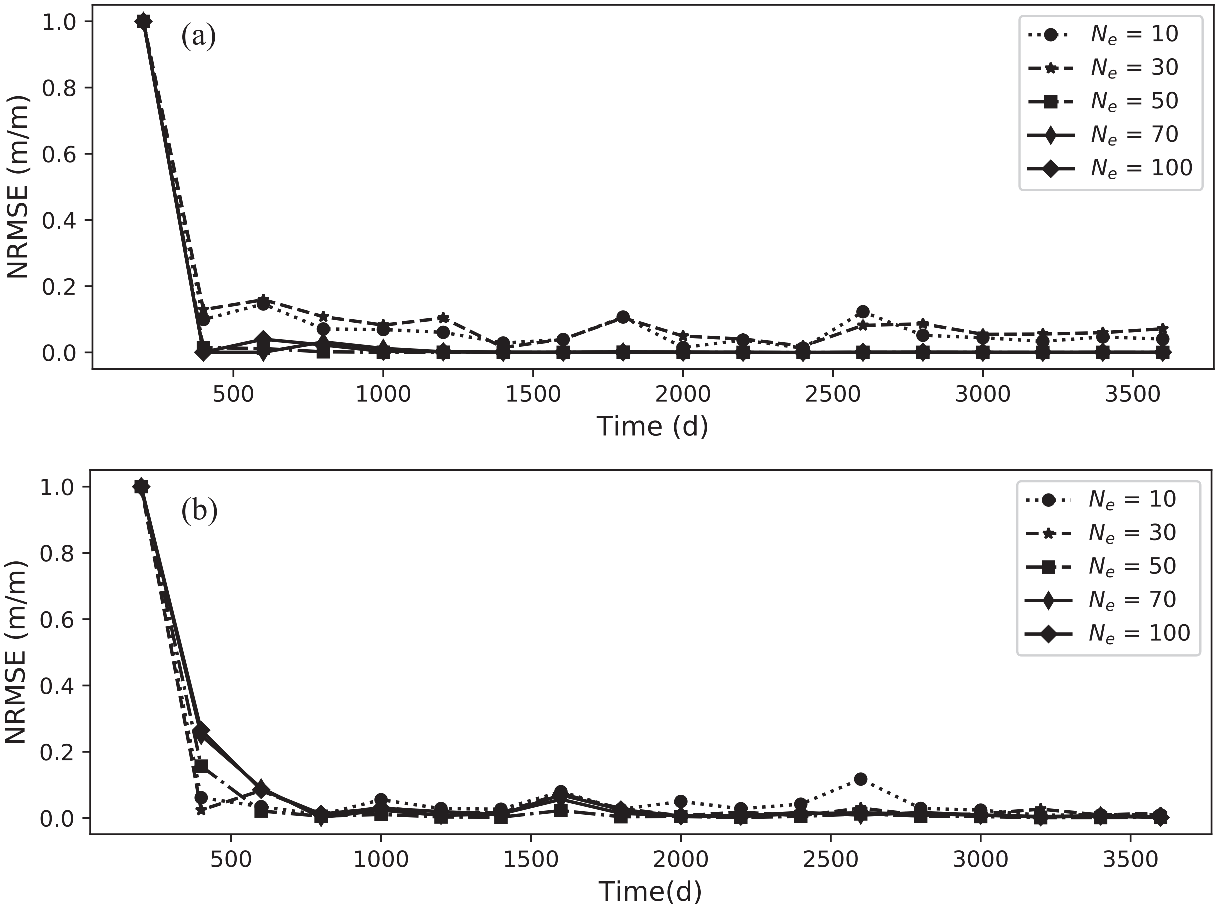

Fig. 17. RMSE estimation of the horizontal nodal displacement for different ensemble size for (a) MC and (b) HS material models.

Appendix B. Algorithm for the Python data assimilation interface with PLAXIS

In this section, a general algorithm (Algorithm 1) of the computation and a partial source code is presented.

Algorithm 1. A general algorithm for the python data assimilation interface with PLAXIS. In this algorithm, *h* is the FEM analysis, and *p* refers to the constant properties during FEM and data assimilation, *i.e.*, geometry and various material properties. For all other symbols see the manuscript.

```
Input: Prior parameter distributions, $D_w$, $p$, $\mathbf{d}$
Output: $\mathbf{Z}^a$, $FoS$
Initialisation                                                        ▷ Python
Read input and define variables                                       ▷ Python
Initialise the state-parameter vectors for all ensemble members       ▷ Python
Develop a connection between Python and PLAXIS                        ▷ Python
while $t \leqslant t_{assim}$ do                                      ▷ Python
    Read water level time series $D_w(t)$
    while $i \leqslant N_e$ do
        Instruct PLAXIS to set up realisation $i$                     ▷ Python
        Instruct PLAXIS to execute realisation $i$ until assimilation time $t$    ▷ Python
        Execute PLAXIS simulation, such that $\boldsymbol{u}_x, FoS = h(\boldsymbol{\theta}, Dw, p)$    ▷ PLAXIS
        Extract required output from PLAXIS (i.e. $\boldsymbol{u}_x$) and develop $\mathbf{Z}^f$    ▷ Python
    Compute data assimilation analysis, $\mathbf{Z}^a = EnKF(\mathbf{Z}^f, \boldsymbol{d}, p)$    ▷ Python
```

B.1. Key elements of source code

```
#1:Initialisation
import numpy as np
import pandas as pd
.
.
.
#2:Read input and define variables
nens=50 #number of ensemble members
tassim=10 #total time steps for data assimilation
e_mean = 25000      #close-to-failure case
e_SD = 5000         #close-to-failure case
phi_mean=20         #close-to-failure case
phi_SD =3           #close-to-failure case
obss = ...         #import (synthetic) measurement data with a noise perturbation
.
.
.
#xpa_e: matrix with prior and estimated "E"
#xpa_phi:  matrix with prior and estimated "phi"
xpa_e=np.zeros((tassim+1, nens), dtype = float)
xpa_phi=np.zeros((tassim+1, nens), dtype = float)
.
.
.
#3:Initialise ensemble members state-parameter vectors
random.seed(seed_number1) #seed_number1: random seed for repeatability
```

```
e_init=[gauss(e_mean, e_SD) for i in range(nens)]
random.seed(seed_number2) #seed_number2: random seed for repeatability
phi_init=[gauss(phi_mean, phi_SD) for i in range(nens)]
xpa_e[0,:]=e_init
xpa_phi[0,:]=phi_init
.
.
#4:Develop a connection between Python and PLAXIS
#s_i is the remote scripting server
#g_i is a variable bound to the global object for PLAXIS input
s_i, g_i = new_server('localhost', localhostport_input,password='PLAXIS_password')
s_o, g_o = new_server('localhost', localhostport_output,password='PLAXIS_password')
.
.
.
while ti<=tassim: #5:While loop for assimilation time steps
    #6:Read water level function Dw(t)
    #Dw=truetransient
    .
    .
    .
    truetransient= ... #list of times and water levels
    ens=1
    while ens<=nens:  #7:while loop for realisations
        #8:Instruct PLAXIS to set up realisation ens
        s_i.new()
        .
        #Create geometry
        .
        .
        .
        #assign the material properties to the soil cluster
        #smodel:constitutive material
        #d_type:drainage type
        #g_uns: unsaturated unit weight
        #g_sat: saturated unit weight
        #nu:Poisson's ratio
        #xpa_e[ti-1,ens-1]*0.5/(1+nu):updated shear modulus for realisation ens
        #c_ref: effective cohesion
        #xpa_phi[ti-1,ens-1]: phi value at time t for realisation ens
        #perx:hydraulic conductivity in x direction
        #pery:hydraulic conductivity in y direction
        material = g_i.soilmat()
        material.setproperties(
            "SoilModel", smodel,
            "DrainageType", d_type,
            "gammaUnsat", g_uns,
            "gammaSat", g_sat,
            "nu", nu,
            "Gref",xpa_e[ti-1,ens-1]*0.5/(1+nu)
            "cref", c_ref,
```

```
            "phi",xpa_phi[ti-1,ens-1],
            "perm_primary_horizontal_axis",perx,
            "perm_vertical_axis",pery
            )
        #Create FEM mesh
        .
        .
        .
        #Set the groundwater level
        .
        .
        .
        #9:Instruct PLAXIS to execute realisation ens until assimilation time t
        #Set initial phase as gravity loading with steady state pore water pressure
        #calculation

        #Define the fully coupled flow-deformation analysis after initial stress phase
        g_i.set (g_i.Phase_1.DeformCalcType, "Fully coupled flow-deformation")
        g_i.set (g_i.Phase_1.TimeInterval, truetransient[-2])
        g_i.set (g_i.WaterSegment_1.TimeDependency, "Time dependent")
        g_i.set (g_i.WaterSegment_1.HeadFunction,g_i.headfunction())
        g_i.set (g_i.HeadFunction_1.Signal, "Table")
        g_i.set (g_i.HeadFunction_1.Table, *truetransient)
        #Create boundary conditions
        .
        .
        .
        #Set the factor of safety calculation phase
        .
        .
        .
        g_i.calculate() #10:Execute PLAXIS analysis

        #11:Extract required output from PLAXIS and develop Zf
        r_X=g_o.getresults(g_o.Phase_1,g_o.ResultTypes.Soil.X,'node')
        r_Y=g_o.getresults(g_o.Phase_1,g_o.ResultTypes.Soil.Y,'node')
        r_Ux=g_o.getresults(g_o.Phase_1,g_o.ResultTypes.Soil.Ux,'node')
        r_Uy=g_o.getresults(g_o.Phase_1,g_o.ResultTypes.Soil.Uy,'node')
        df=pd.DataFrame(zip(r_X,r_Y,r_Ux,r_Uy), colums = ['r_X', 'r_Y', 'r_Ux','r_Uy'])
        dfd=df.drop_duplicates() #deletes data from duplicated nodes
        .
        .
        .
        xf[:,ens-1]=dfd['r_Ux']  #extract the required model state in xf
        ens=ens+1

    #12:Compute data assimilation analysis
    #Augment the state-parameter matrix  for data assimilation
    xsp=np.concatenate((xf, xpa_e[ti-1,:],xpa_phi[ti-1,:]))
    .
    .
```

```
hmat = ...  #hmat:operator to extract the model state at the measurement locations
hmatxf=np.matmul(hmat,xsp) #G*Zft in eq. 27
.
.
pobs = ... #pobs:perturbed observations from imported obss
innovation=pobs-hmatxf #Dt-G*Zft in eq. 27
Czze=np.cov(xsp) #Czze in eq. 25
a1=np.matmul(Czze,hmat.transpose()) # Czze*G^T in eq. 27
.
.
.
k=np.matmul(a1,a4) #a4: inverse of G*Czze*G^T+Cdd in eq 27
xsp=xsp+np.matmul(k,innovation) #estimated state-parameter
.
.
.
xpa_e[ti,:]= xsp[m,:] #extract estimated E in this matrix for time t
xpa_phi[ti,:]=xsp[m+1,:] #extract estimated phi in this matrix for time t
ti=ti+1
```

References

Aanonsen, S.I., Nævdal, G., Oliver, D.S., Reynolds, A.C., Vallès, B., 2009. The ensemble Kalman filter in reservoir engineering-a review. SPE J. 14 (3), 393–412. https://doi.org/10.2118/117274-PA.

Abellán, A., Jaboyedoff, M., Oppikofer, T., Vilaplana, J., 2009. Detection of millimetric deformation using a terrestrial laser scanner: Experiment and application to a rockfall event. Nat. Hazards Earth Syst. Sci. 9 (2), 365–372. https://doi.org/10.5194/nhess-9-365-2009.

Annan, J., Hargreaves, J., Edwards, N., Marsh, R., 2005. Parameter estimation in an intermediate complexity earth system model using an ensemble Kalman filter. Ocean Model. 8 (1–2), 135–154. https://doi.org/10.1016/j.ocemod.2003.12.004.

Bertino, L., Evensen, G., Wackernagel, H., 2003. Sequential data assimilation techniques in oceanography. Int. Stat. Rev. 71 (2), 223–241. https://doi.org/10.1111/j.1751-5823.2003.tb00194.x.

Brinkgreve, R.B.J., Bakker, K.J., Bonnier, P.G., 2006. The relevance of small-strain soil stiffness in numerical simulation of excavation and tunneling projects. In: Proceedings of 6th European Conference in Geotechnical Engineering, Graz, Austria, pp. 133-139.

Burgers, G., van Leeuwen, P.J., Evensen, G., 1998. Analysis scheme in the ensemble Kalman filter. Monthly Weather Rev. 126 (6), 1719–1724. https://doi.org/10.1175/1520-0493(1998)126<1719:ASITEK>2.0.CO;2.

Chen, Y., Zhang, D., 2006. Data assimilation for transient flow in geologic formations via ensemble Kalman filter. Adv. Water Resour. 29 (8), 1107–1122. https://doi.org/10.1016/j.advwatres.2005.09.007.

Evensen, G., 1994. Sequential data assimilation with a nonlinear quasi-geostrophic model using Monte Carlo methods to forecast error statistics. J. Geophys. Res. Oceans 99 (C5), 10143–10162. https://doi.org/10.1029/94JC00572.

Evensen, G., 2009. Data assimilation: The ensemble Kalman filter. Springer Science & Business Media.

Gens, A., Ledesma, A., Alonso, E.E., 1996. Estimation of parameters in geotechnical backanalysis - II. Application to a tunnel excavation problem. Comput. Geotech. 18 (1), 29–46. https://doi.org/10.1016/0266-352X(95)00022-3.

Glegola, M.A., Ditmar, P., Hanea, R.G., Vossepoel, F.C., Arts, R., Klees, R., 2012. Gravimetric monitoring of water influx into a gas reservoir: A numerical study based on the ensemble Kalman filter. SPE J. 17 (1), 163–176. https://doi.org/10.2118/149578-PA.

Hamill, T.M., Mullen, S.L., Snyder, C., Toth, Z., Baumhefner, D.P., 2000. Ensemble forecasting in the short to medium range: Report from a workshop. Bull. Am. Meteorol. Soc. 81 (11), 2653–2664. https://doi.org/10.1175/1520-0477(2000)081<2653:EFITST>2.3.CO;2.

Hou, X., Yang, X., Huang, Q., 2005. Using inclinometers to measure bridge deflection. J. Bridge Eng. 10 (5), 564–569. https://doi.org/10.1061/(ASCE)1084-0702(2005)10:5(564).

Houtekamer, P.L., Mitchell, H.L., 1998. Data assimilation using an ensemble Kalman filter technique. Monthly Weather Rev. 126 (3), 796–811. https://doi.org/10.1175/1520-0493(1998)126<0796:DAUAEK>2.0.CO;2.

Houtekamer, P.L., Mitchell, H.L., 2005. Ensemble Kalman filtering. Quarterly Journal of the Royal Meteorological Society: A Journal of the Atmospheric Sciences, Applied Meteorology and Physical. Oceanography 131 (613), 3269–3289. https://doi.org/10.1256/qj.05.135.

Hsiung, B.C., Dao, S.-D., 2014. Evaluation of constitutive soil models for predicting movements caused by a deep excavation in sands. Electron. J. Geotech. Eng. 19, 17325–17344.

Kalman, R.E., 1960. A new approach to linear filtering and prediction problems. J. Basic Eng. 82 (1), 35–45. https://doi.org/10.1115/1.3662552.

Keppenne, C.L., Rienecker, M.M., 2003. Assimilation of temperature into an isopyc-nal ocean general circulation model using a parallel ensemble Kalman filter. J. Mar. Syst. 40, 363–380. https://doi.org/10.1016/S0924-7963(03)00025-3.

Kim, S., Finno, R.J., 2020. Inverse analysis of Hypoplastic Clay model for computing deformations caused by excavations. Comput. Geotech. 122, 103499. https://doi.org/10.1016/j.compgeo.2020.103499.

Ledesma, A., Gens, A., Alonso, E.E., 1996. Parameter and variance estimation in geotechnical backanalysis using prior information. Int. J. Numer. Analyt. Methods Geomech. 20 (2), 119–141. https://doi.org/10.1002/(SICI)1096-9853(199602)20:2<119::AID-NAG810>3.0.CO;2-L.

Lee, I.-M., Kim, D.-H., 1999. Parameter estimation using extended Bayesian method in tunnelling. Comput. Geotech. 24 (2), 109–124. https://doi.org/10.1016/S0266-352X(98)00031-7.

Liu, K., Vardon, P.J., Hicks, M.A., 2018. Sequential reduction of slope stability uncertainty based on temporal hydraulic measurements via the ensemble Kalman filter. Comput. Geotech. 95, 147–161. https://doi.org/10.1016/j.compgeo.2017.09.019.

Lorentzen, R.J., Fjelde, K.K., Frøyen, J., Lage, A.C., Nævdal, G., Vefring, E.H., 2001. Underbalanced and low-head drilling operations: Real time interpretation of measured data and operational support. In: SPE Annual Technical Conference and Exhibition. https://doi.org/10.2118/71384-MS (SPE-71384-MS).

Lovas, T., Barsi, A., Detrekoi, A., Dunai, L., Csak, Z., Polgar, A., Berenyi, A., Kibedy, Z., Szocs, K., 2008. Terrestrial laser scanning in deformation measurements of structures. Int. Arch. Photogramm. Remote Sens. 37 (B5), 527–531.

Mavritsakis, A., 2017. Evaluation of inverse analysis methods with numerical simulation of slope excavation. MSc thesis. Delft University of Technology, Netherlands.

Miller, R.N., Carter, E.F., Blue, S.T., 1999. Data assimilation into nonlinear stochastic models. Tellus A: Dyn. Meteorol. Oceanogr. 51 (2), 167–194. https://doi.org/10.3402/tellusa.v51i2.12315.

Nævdal, G., Mannseth, T., Vefring, E.H., 2002. Near-well reservoir monitoring through ensemble Kalman filter. In: SPE/DOE Improved Oil Recovery Symposium, (SPE 75235). https://doi.org/10.2118/75235-MS.

Nævdal, G., Johnsen, L.M., Aanonsen, S.I., Vefring, E.H., 2005. Reservoir monitoring and continuous model updating using ensemble Kalman filter. In: SPE Annual Technical Conference and Exhibition. https://doi.org/10.2118/84372-PA (SPE-84372-PA).

Oliver, D.S., Chen, Y., 2011. Recent progress on reservoir history matching: A review. Comput. Geosci. 15 (1), 185–221. https://doi.org/10.1007/s10596-010-9194-2.

Plaxis, 2015. PLAXIS material models manual. Plaxis.

Reichle, R.H., McLaughlin, D.B., Entekhabi, D., 2002. Hydrologic data assimilation with the ensemble Kalman filter. Mon. Weather Rev. 130 (1), 103–114. https://doi.org/10.1175/1520-0493(2002)130<0103:HDAWTE>2.0.CO;2.

Sekhavatian, A., Choobbasti, A.J., 2018. Comparison of constitutive soil models in predicting movements caused by an underground excavation. Int. J. Soil Sci. 13 (1), 18–27 https://doi.org/ijss.2018.18.27.

Skjervheim, J.-A., Evensen, G., 2011. An ensemble smoother for assisted history matching. In: SPE Reservoir Simulation Symposium, (SPE-141929-MS). https://doi.org/10.2118/141929-MS.

Szunyogh, I., Kostelich, E.J., Gyarmati, G., Patil, D., Hunt, B.R., Kalnay, E., Ott, E., Yorke, J.A., 2005. Assessing a local ensemble Kalman filter: Perfect model experiments with the National Centers for Environmental Prediction global model. Tellus A: Dyn. Meteorol. Oceanogr. 57 (4), 528–545. https://doi.org/10.3402/tellusa.v57i4.14721.

Tamura, H., Bacopoulos, P., Wang, D., Hagen, S.C., Kubatko, E.J., 2014. State estimation of tidal hydrodynamics using ensemble Kalman filter. Adv. Water Resour. 63, 45–56. https://doi.org/10.1016/j.advwatres.2013.11.002.

Van Genuchten, M.T., 1980. A closed-form equation for predicting the hydraulic conductivity of unsaturated soils. Soil Sci. Soc. Am. J. 44 (5), 892–898. https://doi.org/10.1139/t66-009.

Vardon, P.J., Liu, K., Hicks, M.A., 2016. Reduction of slope stability uncertainty based on hydraulic measurement via inverse analysis. Georisk: Assessm. Manage. Risk Eng. Syst. Geohazards 10 (3), 223–240. https://doi.org/10.1080/17499518.2016.1180400.

Wang, L., Hwang, J.H., Luo, Z., Juang, C.H., Xiao, J., 2013. Probabilistic back analysis of slope failure - a case study in Taiwan. Comput. Geotech. 51, 12–23. https://doi.org/10.1016/j.compgeo.2013.01.008.

Wösten, J., Lilly, A., Nemes, A., Le Bas, C., 1999. Development and use of a database of hydraulic properties of european soils. Geoderma 90 (3–4), 169–185. https://doi.org/10.1016/S0016-7061(98)00132-3.

Zhou, M., Li, Y., Xiang, Z., Swoboda, G., Cen, Z., 2007. A modified extended Bayesian method for parameter estimation. Tsinghua Sci. Technol. 12 (5), 546–553. https://doi.org/10.1016/S1007-0214(07)70131-1.